POLITECNICO DI TORINO
Dipartimento di Ingegneria Meccanica e Aerospaziale
Master of Science Course
in Aerospace Engineering
Master of Science Thesis

“Optimization of process parameters for DED of IN718 superalloys via Single scan track and single-layer analysis”

Thesis Supervisor

Prof. Sara Biamino

Thesis Advisor

Dr. Abdollah Saboori

Candidate:

Alberto Leo

April 2021

Contents

Chapter 1

Introduction

Additive Manufacturing (AM), together with Big Data science, advanced analytics, robotics and artificial intelligence, is one of the leading sectors of Industry 4.0 (Maci, 2020). The AM has already gained great approval in all these sectors that need flexibility and versatility.

Considering all the types of AM families, Metal AM is one of the most interesting technologies for the Aerospace sector and has attracted the attention of the Leader companies in this field, such as "GE" and "Rolls Royce".

This Master Thesis assignment started from the European Project "4DHybrid", which is based on developing a new concept of Hybrid Additive Manufacturing thanks to the integration of compact, low-cost modules including deposition head, laser source, control and sensors. Many companies such as GE, Siemens, Prima Electro, Optomec, Comau and universities such as Politecnico di Torino, University of Birmingham and SUPSI takes part in this project.

The main goal of this work is to identify the best process parameters for the Nickel-based Superalloys IN718 samples produced via Directed Energy Deposition (DED) process. In order to reach this objective have been analyzed a different kind of features such as IN718 Single Scan Tracks (SSTs), Single Layers (SLs), and Bulks (Blks) deposited on a not pre-heated IN718 substrate.

First of all, it is reported bibliographic research in order to introduce the overall framework of the AM features and its applications in the Aerospace-Aviation field. Additionally, a comparison between the two main Metal AM families, Powder Bed Fusion (PBF) and Directed Energy Deposition (DED) is reported to evaluate the advantages and disadvantages of each type of technology as well as their process hallmarks and parameters.

Secondly, the main features, composition and applications of the Nickel-based Superalloys are explained. Moreover, the relationship between IN718 and AM processes are described.

Thirdly, it is reported a "Material and Methods" overview in order to explain how practically the results of this assignment are obtained.

Finally, the results concerning the analyzed features are reported and discussed in terms of their Morphological and Microstructural aspects, as well as their Defectology. At the end, the main conclusions of this work are presented as "conclusions".

Chapter 2

Metal Additive Manufacturing

2.1 Introduction

In the past few years, Additive Manufacturing (AM) began to arise interest in the industrial environment thanks to its versatility, the high utilization of materials and the reduction of production time.

The ISO/ASTM 52900 norm (Bahnini et al., 2018) defines Additive Manufacturing as "the process of joining materials to make parts from 3D model data, usually layer upon layer, as opposed to subtractive manufacturing and formative manufacturing methodologies."

According to this definition, it is possible to understand the difference between the AM and the actual production system, the Subtractive Manufacturing, based on casting or material removal with milling, turning and drilling processes where several manufacturing restraints must be respected (Bacciaglia et al., 2020).

The main fields of application of AM are the Aerospace and Aviation sectors. Both these areas appreciate the main hallmarks of AM, which are the production of very complex parts at low cost and the relatively inexpensive production of small lots. AM also allows the opportunity to optimize the Nickel-based superalloys, widely used in the Aerospace sector, in weight, performance, damage tolerance and assembly simplification.

2.2 AM classification

Nowadays, there are several kinds of AM processes, each with its own peculiarities, limitations and advantages. The ASTM Standards classified all the processes, materials and technologies in a rigorous way, as exposed in Fig. 2.1 (ISO/ASTM 52900:2015 (ASTM International, 2016)).

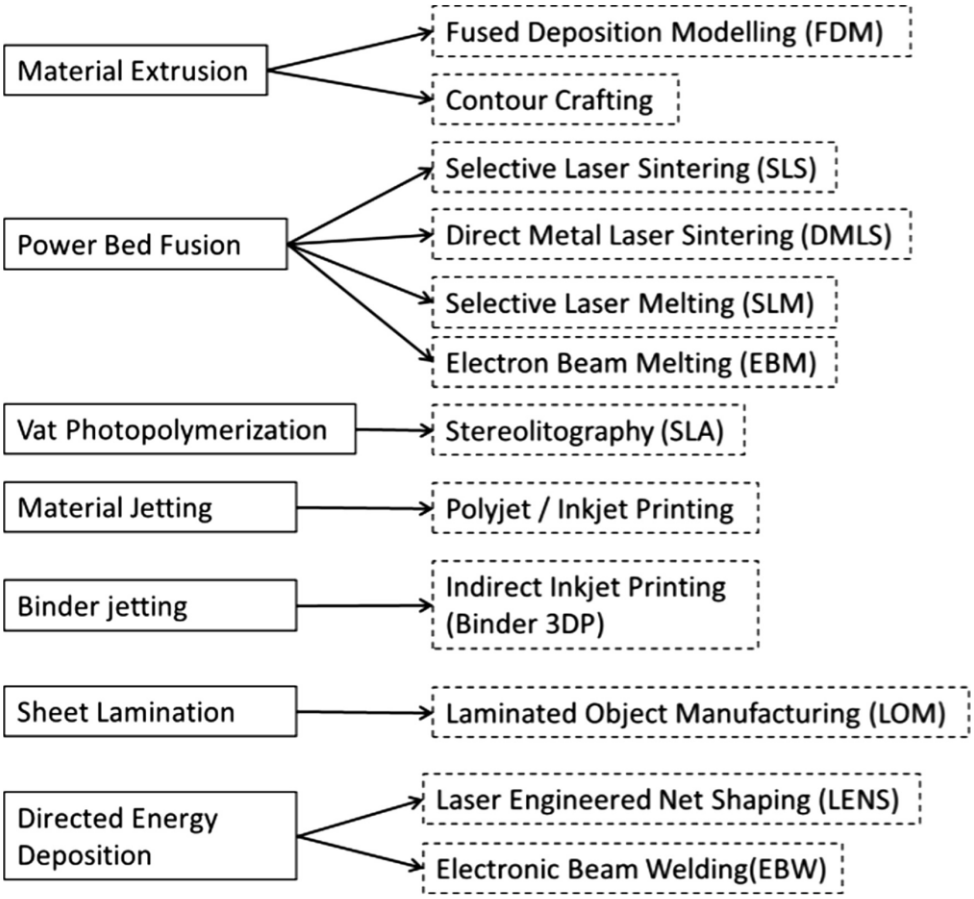

Fig. 2.1: ASTM terminology for AM processes

The main AM technologies are (Bacciaglia et al., 2020):

- Fused Deposition Modelling (FDM)
- Selective Laser Sintering (SLS)
- Selective Laser Melting (SLM)
- Electron Beam Melting (EBM)
- Stereolithography (SLA)
- Polyjet/Inkjet Printing
- Directed Energy Deposition (DED)

These technologies offer a great variety of operating philosophies, material properties and production strategies, which reflect on the production time, costs, quality and mechanical properties.

The technologies most commonly used in the Aerospace field are:

- Powder Bed Fusion: uses thermal energy to fuse regions of a powder bed selectively
- Directed Energy Deposition: uses focused thermal energy (e.g. laser, electron beam, plasma arc) to melt the materials as they are being deposited

However, after finishing the fabrication with the AM process, parts are not ready for end-use applications and require some post-processing operations before their intended use (Bahnini et al., 2018).

2.3 AM Advantages and Disadvantages

2.3.1 Advantages

The increasing usage of AM technologies is aligned to its many advantages, such as (Attaran, 2017; Bacciaglia et al., 2020; Johnson et al., 2017; Wimpenny et al., 2016):

- *Design Flexibility*: AM offers high flexibility on the components' design in terms of shape and geometries, thanks to the reduction of manufacturing constraints.
- *Minimization of Internal Process Logistic*: AM can reduce the time needed for the design-to-manufacturing cycle, additionally, it contributes to the minimization of internal process logistics due to significantly less operations. 3D printing can also be used to manufacture prototype parts well before the production, thus saving time, effort and money. This particular feature is very important for companies as the cost of changes in the products' design cycle increases within the development phase.
- *Product Customization*: its extreme design flexibility allows custom shapes to be produced. This is an important aspect for every industry that requires high customization at a low volume production rate such as the biomedical industry, the space industry or even racing and classic cars.
- *Material Customization*: it is possible to customize the material used to produce a component in many ways (e.g. to create custom mixes of powder, to embed fibres in a plastic filament, to increase the material strength with carbon fibres or wood fibres; to use bio-compatibles materials). If a material that suits the needs is not available, it is possible to replace it with a component with the required material property produced by changing the internal porosity with the adoption of functionally graded materials, or cellular structures. This is possible thanks to the use of cellular structures like foams, honeycombs and lattices. Fig. 2.2 shows the complexity of the shapes of lattice structures. Seems clear that may arise several problems if it is used a traditional manufacturing process.

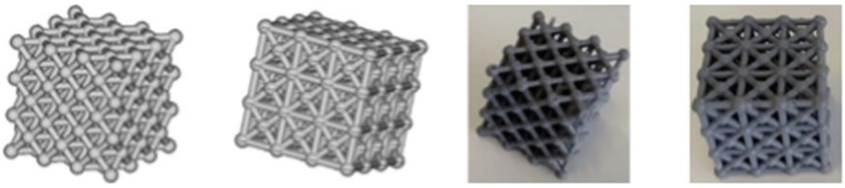

Fig. 2.2: Uniform lattice CAD models on the left and 3D printing in the right with SLA techniques (Bacciaglia et al., 2020)

- *Topology optimization (TO)*: it is a numerical procedure where the shape of a body is changed automatically with the use of a fitness function that is identified in the stress, compliance or maximum displacement. Using an iterative procedure based on the Finite Element Analysis (FEA), the output of the algorithm is a material distribution, which minimizes the fitness function (Fig. 2.3). The obtained object presents a complicated shape, which is impossible to reach by using the traditional manufacturing processes, and it is hard to imagine by a human designer. The use of 3D printing together with TO can gather enormous advantages (e.g. reduced quantity of wasted materials, time savings, weight reductions), especially in the aerospace sector.

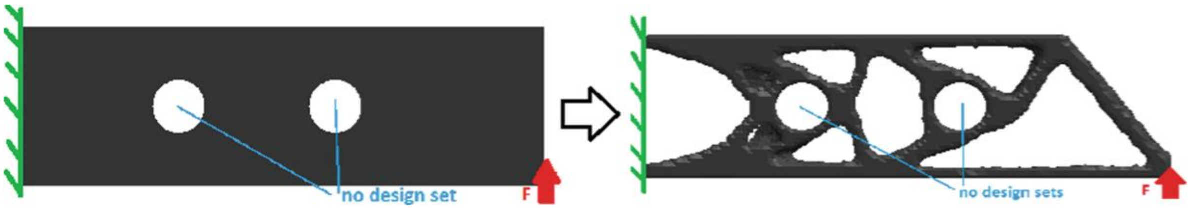

Fig.2.3: Cantilever beam optimized through TO algorithm (Bacciaglia et al., 2020)

- *Less Economical Effort*: it is possible to manufacture parts with a wide range of dimensions, geometries and materials with a single AM machine. This is very important for small companies that could invest in an AM machine, which has a small capital compared to a more expensive entire supply chain based on traditional manufacturing. In addition, as previously mentioned the production of small lots is relatively inexpensive.

- *Assembly Connection Minimization*: by using AM, it is possible to generate complex geometries in one piece instead of an assembly of multiple parts. In this way, there is a reduction of the time needed for proper bolting connections or part welding. Moreover, one-piece parts are safer in respect to an assembly of bolted parts: connections are critical in a vibrating environment, and the maintenance operations are very expensive.
- *Multi-Material Capability*: the AM machines could use several materials in a single component. This multi-material and multi-structure freedom can give to the additive manufacturing a very competitive advantage over traditional processes. (Bacciaglia et al., 2020).

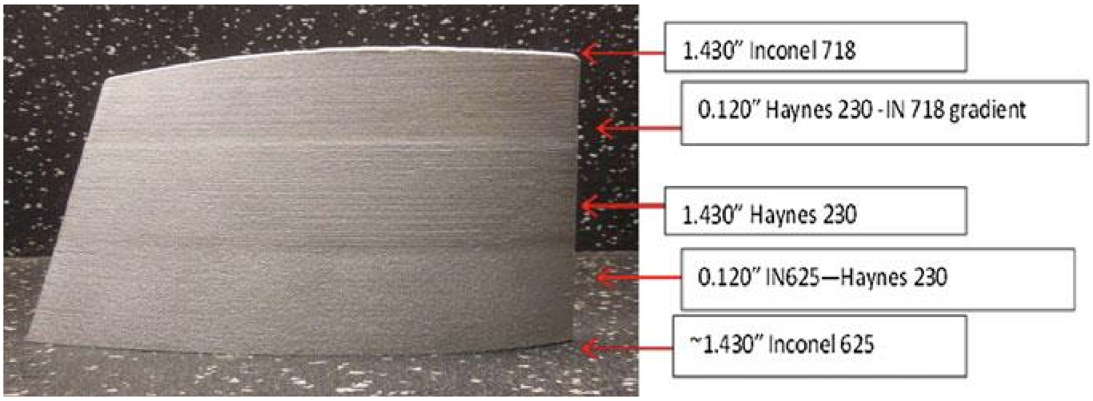

Fig.2.4 Aerofoil with multi alloy deposition (Inconel-Haynes-Inconel using LMD) (Wimpenny et al., 2016)

- *Reduction of repairing times*: by using AM, it is possible to add new layers on the damaged parts simply. In this way, it is not necessary to replace the component, thus resulting in a reduction of costs and time.
- *Manufacturing decentralization*: manufacturing in remote locations and goods delivery is no longer a restriction.
- *High material utilization (90-95%)*: the only wasted material is the one removed in the post-processing operation. This feature is very important in the aerospace industry due to the high material cost.

2.3.2. Disadvantages

In this section the main drawbacks and weaknesses of AM technologies will be discussed, such as (Attaran, 2017; Bacciaglia et al., 2020):

- *Anisotropic material*: the resulting component after an AM process presents a high anisotropic level because of the process itself. This could be problematic in many structural applications, and this applies to various kind of AM processes.
- *Surface roughness*: if an FDM machine is not accurate enough, each slice could be seen at naked eye. This is one of the main reason why post-processing operations are necessary.
- *CAD software still shows large limitations*: common design tools available to the engineer shows limitations, in general, within all the applications when the external surface is quite complex (such as lattice structures). Moreover, all the software tools used are separate from each other, and an end-to-end workflow capability is still missing.
- *Limited material portfolio and limited building size*: AM still use a limited amount of materials compared to the traditional manufacturing processes. Furthermore, 3D printers have a limited size of produced components: the largest printing chambers have a volume of 1 m^3, and this is a limiting factor for applications in which components with larger dimensions are involved.

- *Inspection and maintenance*: making a complex assembly in one single piece is certainly advantageous but could create some problems in the case of maintenance and repair operations. Before replacing a whole component with a higher economic impact, a pros & cons analysis should be carried out depending on the single application (Bacciaglia et al., 2020).
- *High costs*: in AM the costs per unit does not depend on the production rates therefore, an increase in production rates does not correspond to a reduction in cost per unit, making traditional manufacturing more attractive. We also need to consider the upfront capital expenditures for AM machines which are quite high compared to traditional milling and turning machines (800 k€ for a SLM AM machine; 200 k€ for a traditional CNC). We should also take into account that materials for AM, the adoption of an inert atmosphere or keeping a vacuum regime within the chamber are generally expensive.
- *High production times*: this problem is noticed when serial production in short times is requested. Therefore, there is the need to estimate, for every single application, the breakpoint value for which AM is more convenient with respect to traditional processes.
- *Slow certification process*: AM is a relatively new technology and a limited amount of information is available to understand the material behaviour during its operative life when fatigue analysis plays a fundamental role (Bacciaglia et al., 2020). In the aerospace sector, the application of AM is still focused on non-safety-critical components and cannot be used for structural parts.

2.4 Metal AM categories

The Metal AM is the most promising amongst all the AM families thanks to the combination of freedom manufacturing gained by 3D printing and the metal thermos-physical properties. Thanks to this mixture of features, it is possible to realize very complex parts capable of enduring in severe conditions of loads and thermal phenomena while ensuring some essential functionalities such as thermal and electrical conductivity. Furthermore, metal AM allows the production of unique parts while embedding a large amount of sophisticated features making obsolete the need to build several components to be respectively assembled. In this way it is possible to realize parts which are ultimately less expensive, more lightweight and with performing physical-mechanical properties (Yu et al., 2020). Thanks to these hallmarks, Metal AM is broadly employed in sectors such as aviation, aerospace and automotive, where performances optimization and weight reduction are the main research fields.

Generally speaking, the creation of the part is performed starting from a feedstock material in powder or wire form, then melted by a laser or an electron beam melting source and made by solidifying overlapped layers successively deposited.

The two most common AM technologies for aerospace applications are DED and PBF.

DED technologies include:

- Laser Metal Deposition (LMD)
- Laser Engineering Net-Shaping (LENS)
- Electron Beam Welding (EBW)
- Electron Beam Free-Form Fabrication (EBF^3)
- Wire Arc AM (WAAM)

PBF technologies include:

- Direct Metal Laser Sintering (DMLS)
- Selective Laser Melting (SLM)
- Electron Beam Melting (EBM)

Other Metal AM processes:

- Binding Jet (BJ)
- Cold Spraying (CS)
- Friction Stir Welding (FSW)
- Sheet Lamination (SL)

2.4.1 Direct Energy Deposition

DED technology works by simultaneously feed and melt material on a platform, usually occurring with an inert gas atmosphere. The feedstock is typically a powder or a wire and is melted using a focused energy source such as electron beams, laser beams and arcs. DED technology can be implemented in a multiaxial machine and provide a 3D positioning. In this way it is possible to realize complex parts without the need for support structures (Najmon et al., 2019). This high versatility in orientation makes the DED technology ideal for the component repair of turbine blades, engine combustion chambers, compressors, airfoils and blisks. Turbine airfoils have been repaired to 0.030 mm accuracy from the original blade and show that for a 10% repair there is at least a 45% improvement in the carbon footprint and a 36% of total energy savings (Wilson et al., 2014). The mechanical properties are highly influenced by the process parameters, load directions and post-processing operations. These systems generally have larger building volumes. The differences between these machines tipically include changes in laser power, laser spot size, laser type, powder delivery method, inert gas delivery method, feedback control scheme and/or the type of motion control utilized (Gibson et al., 2015). Ni-based alloys have been typically used in the fabrication of AM parts via DED technology.

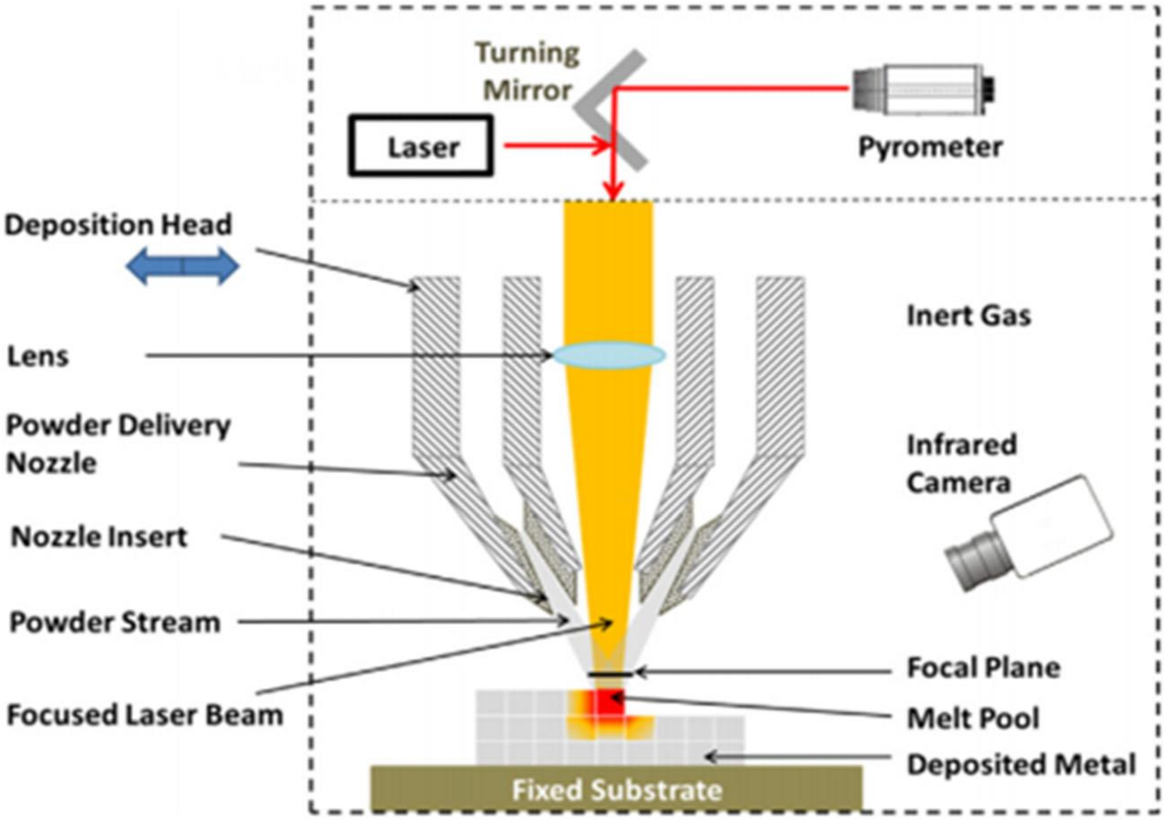

Fig. 2.5: A schematic of Powder Feed Fusion System (Bahnini et al., 2018)

We can divide the DED systems into two categories based on the feedstock material form employed to be melted and welded with the substrate or with the already solidified deposited layers (Gibson et al., 2015). These are also known as the “Wire” DED system (Wire Feeding), and the “Blown Powder” DED system (Powder Feeding).

2.4.1.1 DED-Wire Feeding

The deposition by WAAM can occur either in the atmosphere using a shielding gas or in a sealed chamber with a controlled atmosphere. In both cases there is a high building freedom thanks to a robotic arm that manages the deposition tools, while sophisticated transductors and sensors control the process performances and the process parameters (Wu et al., 2018).

The deposition process starts when a laser or an electron beam source melts the wire feedstock to the substrate creating the first layer; subsequently, the part is realized by over positioning successive layers forming a 3D component.

By using WAAM techniques, we could realize not-excessively complex parts, with no porosity imputable to the process and a material utilization close to 100%. However, the dimensional accuracy and the surface finishing result to be very meagre and a post-process subtractive operation is necessary before the implementation of the component in its applications. For these reasons, this technique is generally used to realize structural and functional parts (Gibson et al., 2015).

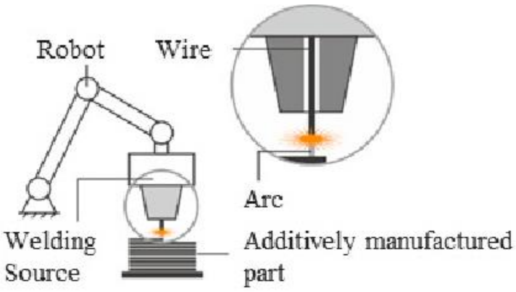

Fig. 2.6: General scheme of Wire Arc Additive Manufacturing (WAAM) techniques (Ünsal et al., 2020)

2.4.1.2 DED-Powder Feeding-LBMD

This technique uses a main nozzle mounted into a two or three-axis mechanic arm system, in which is embedded the primary energy source (usually an Nd-YAG or CO2 laser, or an electron beam). In addition, also the building plate is tied to a separate mechanic system with two or three freedom degrees. The combination of the primary mechanic arm and the base plate overall allow a nine-freedom degrees system (Zenou & Grainger, 2018).

The deposition head embeds a feeding system composed of one or multiple channels, creating a mixture of metal powder and carrier gas in conjunction with shielding gas. The shielding gas plays a fundamental role in preventing the embedding of impurities, as well as the material oxidation, regardless of whether the deposition takes place in the atmosphere or not. The substrate melts, creating a Melt Pool due to the interaction between the laser source and the plate, and the fluxing particles become entrapped (Gibson et al., 2015).

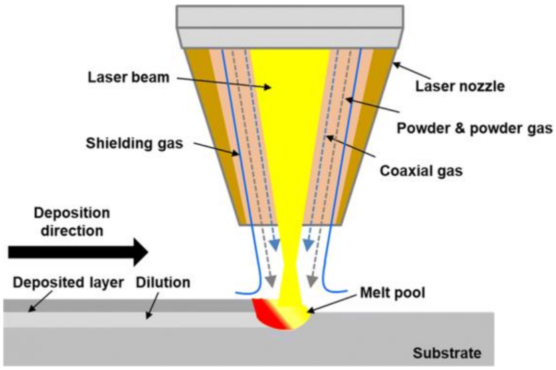

Fig. 2.7: Scheme of a Laser Beam Metal Deposition (LBMD) technique (Oh et al., 2020)

The mechanical properties and the microstructure of the LMDB process are highly related to the process parameters setting (Johnson et al., 2017; Mahamood & Akinlabi, 2018):

- Transverse Speed (1-20 mm/s): directly affects the tracks' profile, width and cooling rate. A high transverse speed leads to high cooling rates promoting fine and columnar grains' growth, whereas modest transverse speed values produce low cooling rates responsible for a coarse microstructure.
- Laser Power (100-5000 W): directly affects the cooling rate and the microstructure. In contrast to transverse speeds, a high level of laser power promotes coarse microstructure, while modest laser energy results in fine, columnar microstructures. However, to have a more accurate analysis, it is necessary to consider the real energy absorbed by the material, not taking account of the reflected radiation.
- Powder Flow Rate: directly affects the deposit homogeneity and compliance. This is the hardest parameter to evaluate because of the difficulty to make this parameter predictable. It is usually considered as a constant variable.
- Laser Beam and Powder Stream: directly affect the layers' height and boundary conditions. It considers the dynamic coupling of powder stream and laser beam.

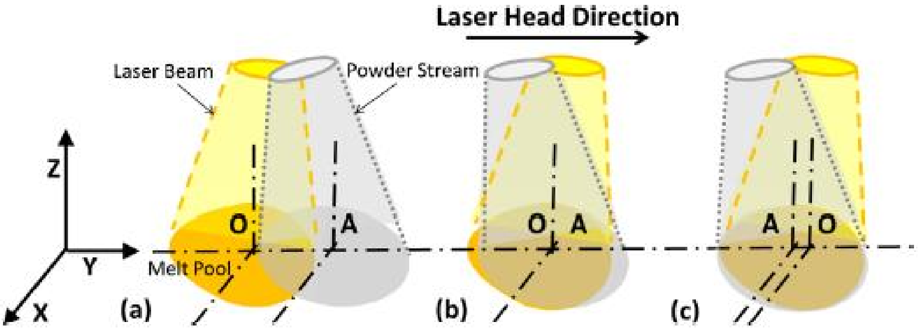

Fig. 2.8: Laser beam and powder stream dynamic configurations (Di Falco, 2019)

- Hatching Strategy: it considers the path followed by the deposition head in a 2D area. This parameter highly influences the residual stress, the eventual part deflection and the thermal distortion.

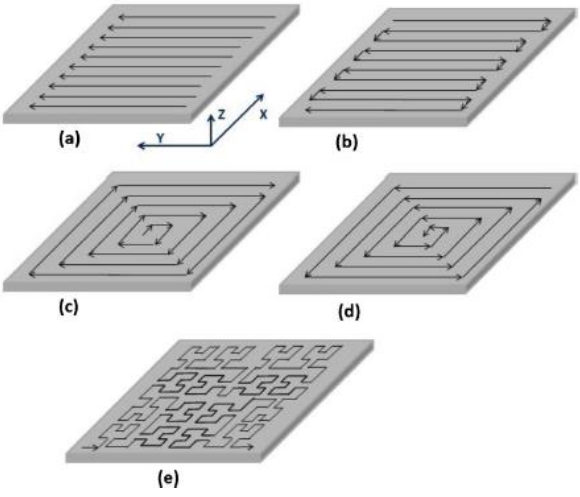

Fig. 2.9: Scanning strategies (Johnson et al., 2017)

2.4.2 Powder Bed Fusion

PBF technologies work by locally melting powder on a substrate to form layers. A levelling roller spreads a thin layer of powder over the platform while a moving energy source melts the powder into successive cross-sections according to the CAD file. The first layer formed adheres to the built plate (pre-heated or not) which is generally constituted by the same material of the part building. Once the layer is finished, the platform goes down a pitch equal to the layers' thickness; the levelling roller spreads another amount of powder over the solidified layer and the building process is repeated (Bahnini et al., 2018). The process is iteratively repeated until the finished part is formed.

In the PBF process is not necessary a supporting structure because the un-melted powder acts as a support to the part being built and could be reused. An inert gas atmosphere should be used, in SLM and DMLS, to avoid powder oxidation, while for the EBM, its better use a vacuum chamber. For this reason, the EBM technology finds considerable applications in the space field. Titanium alloy (Ti-6Al-4V) was commonly used in the manufacture of AM parts via EBM technology.

By using PBF processes, it is possible to create internal passage and obtain higher-fidelity built features if compared to DED processes (Frazier, 2014).

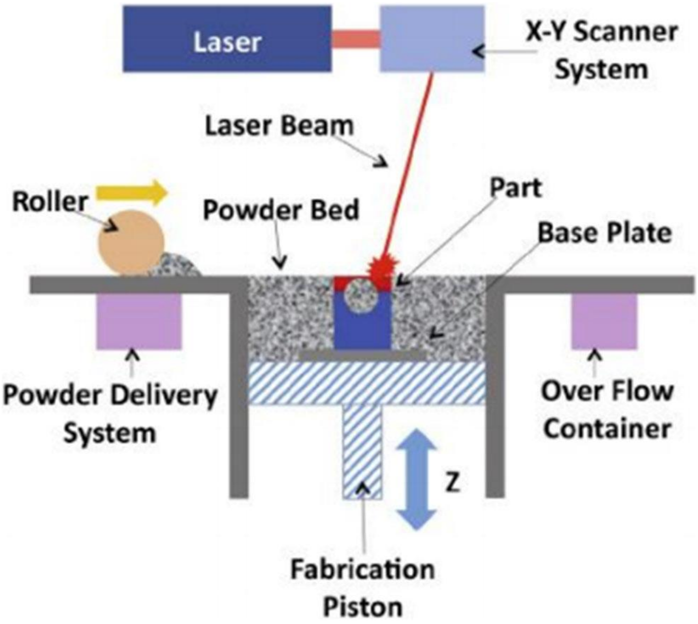

Fig. 2.10: Powder Bed Fusion system (Bahnini et al., 2018)

2.4.3 DED and PBF comparison

A comparison of the main metal AM categories is shown below. It considers the general differences between process parameters and equipment capabilities.

Tab. 2.1: Comparison of LMD, SLM and EBM (Di Falco, 2019)

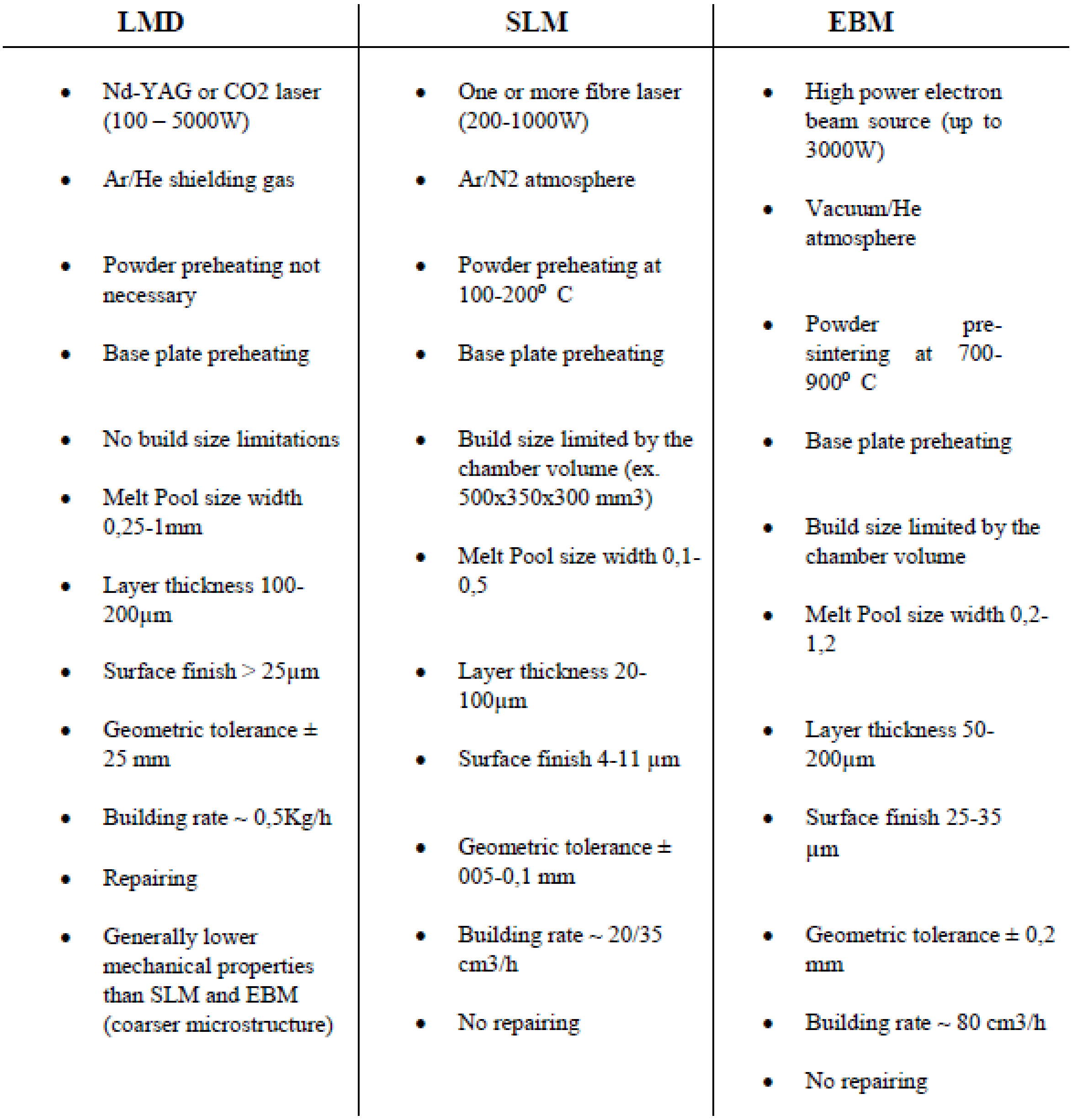

LMD	SLM	EBM
• Nd-YAG or CO2 laser (100 – 5000W)	• One or more fibre laser (200-1000W)	• High power electron beam source (up to 3000W)
• Ar/He shielding gas	• Ar/N2 atmosphere	• Vacuum/He atmosphere
• Powder preheating not necessary	• Powder preheating at 100-200° C	• Powder pre-sintering at 700-900° C
• Base plate preheating	• Base plate preheating	• Base plate preheating
• No build size limitations	• Build size limited by the chamber volume (ex. 500x350x300 mm3)	• Build size limited by the chamber volume
• Melt Pool size width 0,25-1mm	• Melt Pool size width 0,1-0,5	• Melt Pool size width 0,2-1,2
• Layer thickness 100-200µm	• Layer thickness 20-100µm	• Layer thickness 50-200µm
• Surface finish > 25µm	• Surface finish 4-11 µm	• Surface finish 25-35 µm
• Geometric tolerance ± 25 mm	• Geometric tolerance ± 005-0,1 mm	• Geometric tolerance ± 0,2 mm
• Building rate ~ 0,5Kg/h	• Building rate ~ 20/35 cm3/h	• Building rate ~ 80 cm3/h
• Repairing	• No repairing	• No repairing
• Generally lower mechanical properties than SLM and EBM (coarser microstructure)		

2.5 Metal AM Applications

As seen in the previous sections, Metal AM have several applications in sectors with small production lots, high degree of customization and low-cost prototypes. For this reasons AM is perfect for the aerospace, automotive and bio-medical fields.

2.5.1 Aeronautical applications

AM finds various applications in the aerospace field especially for the repair of components using LMD. Furthermore, by using more current machining there is an extreme waste of highly expensive material because only 5% of the original material is the content in the finished part. Some examples of AM uses are outlined below.

- *GE Aviation - Leap Engine Fuel Nozzle*
  GE has been working on AM technology for many years and has successfully produced the Leap Engine Fuel Nozzle in cobalt chrome by laser AM melting process. This is a unique component and has replaced an assembly of 20 components without joints ensuring a reduction in cost, weight and improved performance (Wimpenny et al., 2016). On each Leap Engine there are 19 fuel nozzles.

Fig. 2.12: AM Leap Engine fuel nozzle

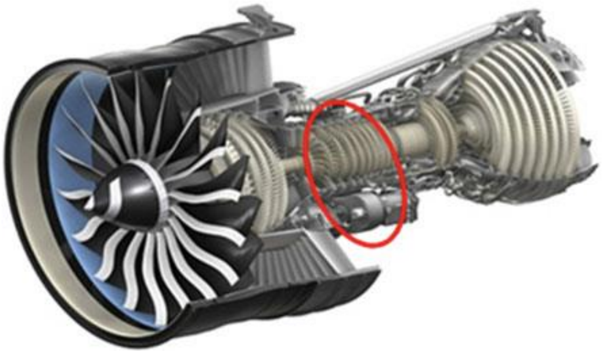

Fig. 2.13: Leap Engine

- *SAFRAN R&D Engine Components*
  SAFRAN Group uses AM for a number of engine components for development of engines and prototypes for both Turbomeca and Snecma. In particular, Snecma uses AM for the guide vanes of the silver-crest business jet engine and for the manifold of the hydrogen turbo pump mounted on the Vinci rocket engine. Furthermore, Snecma uses AM for repairing operations and for the speedy implementation of design changes.

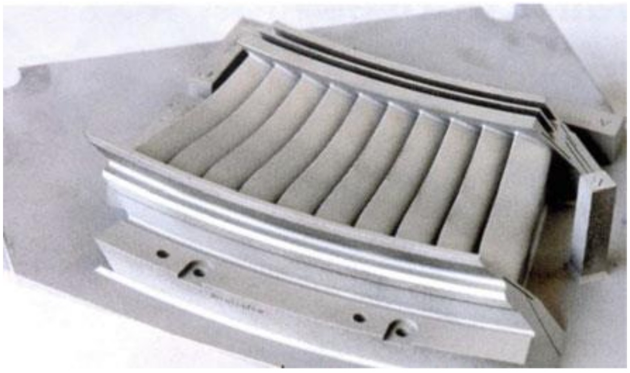

Fig. 2.14: Engine stator vane (Wimpenny et al., 2016)

- *Airbus A350 XWB cabin bracket connector*
  Airbus uses Laser CUSING (Concept Laser GmbH) technology for the production of A350 XWB cabin bracket connector. This component is made out of Titanium powder with more than 30% weight reduction, a percentage of wasted material of only 5% and a 5 months reduction of production time.

Fig. 2.15: Cabin bracket of the A350 XWB manufactured using the laser CUSING technology

- *Boeing*
  The use of AM technologies by Boeing is increasing rapidly in the last years. The company spokesman Nathan Hulings says “We have approximately 300 different part numbers on 10 different aircraft production programs, which amounts to more than 20,000 non-metallic additive manufactured parts that are on vehicles that we have delivered to our customers”. (Krassenstein, n.d.). On the F/A-18 Super Hornet there are approximatively 150 parts produced through SLS.
- *RR Trent XWB-97*
  Rolls-Royce uses 3D Printing for the front bearing housing of the RR Trent XWB-97 engine. This part measures 1.5 m in diameter, is 0.5 m thick, and holds 48 aerofoils manufactured using EBM technology.
  RR estimates a 30% of saved manufacturing time due to the use of AM instead of traditional manufacturing methods.

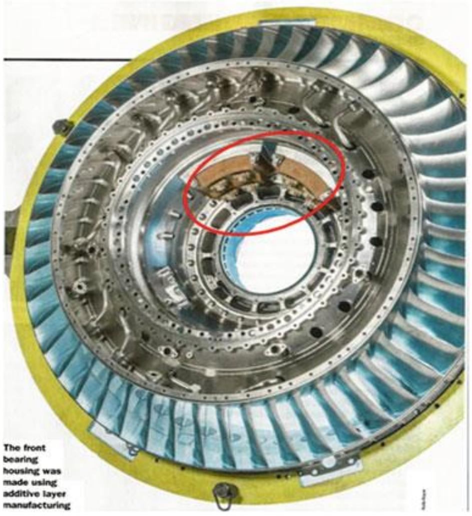

Fig. 2.16: RR Trent XWB-97 front bearing housing

- *P&W PP P1500G*
  Pratt & Whitney uses AM technologies to produce some components, such as compressor stators and sync ring brackets, for their Pure Power PW1500G engine. The Bombardier CSeries passenger aircraft uses this engine. By using AM processes, P&W achieved a 50% weight reduction in a single part and saved 15 months lead-time compared to the conventional manufacturing methods.

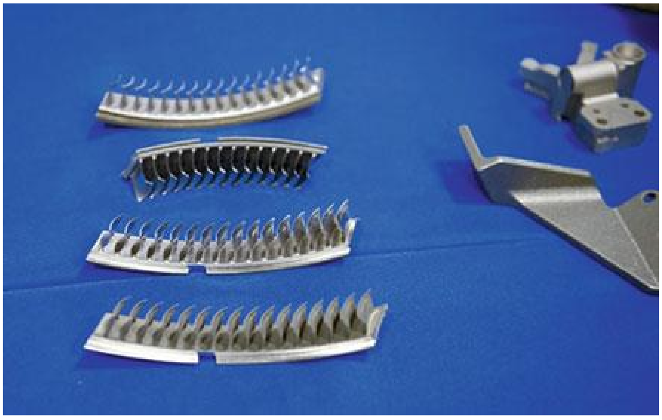

Fig. 2.17: 3D printed P&W's compressor stators

2.5.2 Space applications

In recent years, agencies like NASA and ESA have been conducting research on possible applications of AM for in space operations, from using it to print ceramics to printing CubeSat propulsion systems, to using laser engineered net shaping (LENS) with lunar and Martian regolith, to potentially printing an entire spacecraft in orbit (Sacco & Moon, 2019). However, mass use of AM in the space industry has not occurred yet due to the difficulty in modelling the manufacturing process and predicting the properties of printed parts.

Private companies such as Thales Alenia Aerospace (TAS), Boeing, Space-X and Airbus are also working on AM for space, but as they did not release sensitive information to the public, it is difficult to go into much detail.

When discussing 3D Printing for space, it is important to specify that not all research is done on the Earth, some has been done in space on the International Space Station (ISS). This is possible thanks to two Fuse Deposition Modelling (FDM) small printer, the 3DPrint and the AMF (Additive Manufacturing Facility). A comparison between the flight AMF samples with the ground ones shows that microgravity seems to produce parts with the worst compressive and flexural properties but better tensile.

Tab. 2.2 Tests on samples prepared in orbit (0 g) and on the ground (1 g) (Prater et al., 2016; Thomas et al., 2017).

Environment	0 g		1g		
Printer	3DPrint	AMF	3DPrint	AMF	Test Type
Ultimate strength [MPa]	45.1	58.9	35.9	62.3	Flexural
Elastic modulus [GPa]	1.7	1.9	1.4	2.1	Flexural
Ultimate strength [MPa]	27.9	38.0	23.9	37.8	Tensile
Elastic modulus [GPa]	1.7	3.1	1.5	2.2	Tensile
Ultimate strength [MPa]	38.5	51.1	51.4	52.9	Compressive
Elastic modulus [GPa]	1.1	1.7	1.7	1.5	Compressive

The ultimate goal of in space manufacturing (ISM) is to manufacture and assemble large structures in orbit. Tethers Unlimited, Inc. (TUI) proposed a solution for ISM of large structures: a suite of technologies called SpiderFab that uses a combination of 3DP and on-orbit robot assembly to create structures such as antenna reflectors, solar sails, solar concentrators and manned habitats.

Fig. 2.18: Concept art of SpiderFab Bot (Hoyt et al., 2013)

It is important to specify that ISM mainly use polymers instead of metal. This is due to the fact that most metals required heat treating to achieve their full properties, which is very difficult to conduct in space. Polymers have the advantage of requiring a lower printing temperature reducing the amount of power required by the spacecraft.

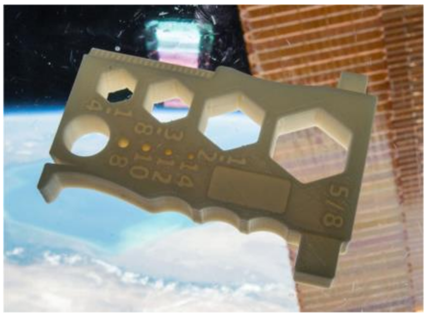

Fig. 2.19: Multipurpose Precision Maintenance Tool (MPMT) printed on the ISS

- *NASA - Complex Rocket Injector*
  NASA uses SLM to produce the rocket injector of the Space Launch System (SLS) J-2X engine. It is processed using a nickel-chromium alloy powder and is composed of only two parts while the

traditionally manufactured injector had 115 parts. Furthermore, AM process reduced the manufacturing time from months to weeks.

Fig. 2.20: NASA Rocket Injector

- *Airbus Defence and Space*
  In the space sector, AM is used on the latest generation of satellites from Airbus Defence and Space. In particular, it is used on the titanium brackets, which need to withstand the high range of temperature (330 °C), and external forces (20 kN) without problems. Furthermore, the utilization of 3D printing has allowed a reduction of the production time by 5 days, production saving over 20% and a significant weight reduction of the component.

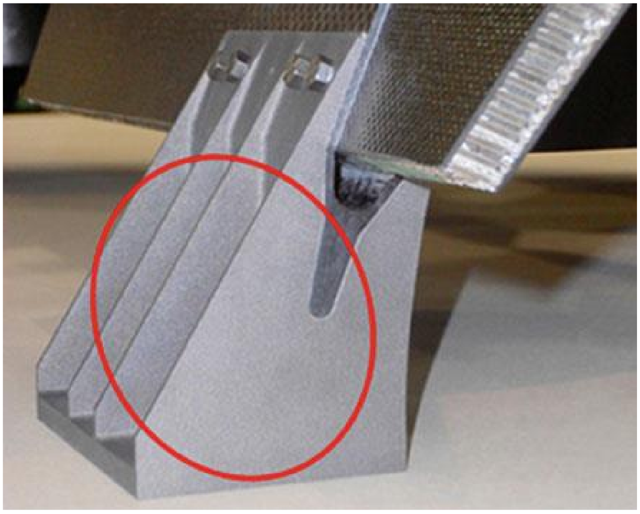

Fig. 2.21: 3D printed titanium brackets

2.5.3 Automotive applications

One of the first applications of 3D Printing was in the automotive industry. General Motors has been using AM to manufacture prototypes for over 20 years to accelerate time to market and reduce the cost associated with product development. (Attaran, 2017). However, AM has other uses besides prototyping in the automotive industry. In 2013, Kor Ecologic introduced the Urbee, the first electric car with fully printed interior and exterior. In this way, it is possible to remove excess parts that cause drags and add weight. While the car is currently a prototype, the company is working on the Urbee 2 for consumer use.

“More and more companies are adopting 3D printing for masks and equipment”, says Ron Clemons, director of business development at Stratasys Direct Manufacturing. “Masks and 3D printing devices can reduce costs, provide lighter and more ergonomic tools and more. In addition, 3D printing showed a significant reduction in lead time from 40% to 90% and a cost reduction of up to 60%. 3D printing tools also allow design teams to save time because they can be more responsive with the ability to create custom one-off components.”

Some example of AM uses are outlined below.

- *Volkswagen*
  The German car manufacturer has redesigned a support for front windows that weighs 74% less than the original part.
- *Audi*
  In 2017, AUDI inaugurated a 3D printing centre in Ingolstadt, Germany and collaborates with SLM Solutions Group AG, a company specialized in the production of metal additives, for the production of prototypes and spare parts.
- *Rolls Royce*
  The British automaker uses 3D printing to print components for their fleet's flagship, the Phantom. More than 10,000 components have already been printed.
- *Porsche*
  Porsche is leveraging 3D printing technology to create spare parts for its cars, combining SLM printing technology for metal parts and SLS for plastic parts and equipment.
- *Formula 1*
  In the racing world, there are several applications of AM technologies. The ability to create innovative geometries in a short time makes 3D printing technology a must for research and study in wind tunnel. Both 3D SLA and SLS printing systems are used for the realization of wings/ailerons, parts of the braking system, cover of suspension and engine parts, internal pipelines and deflectors.

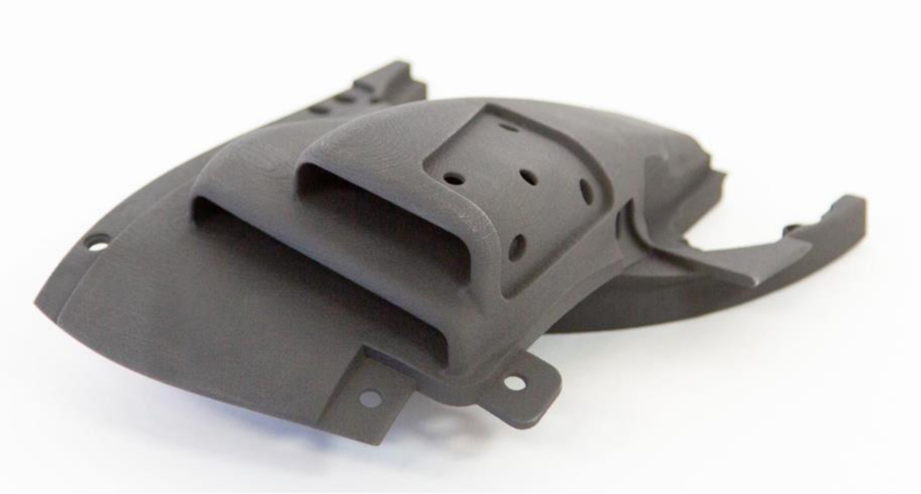

Fig: 2.22: brake air intake

2.5.4 Bio-Medical applications

The AM has revolutionized the medical industry. By using 3D Printing it is now possible to scan a patient using CAD software, realize a tailored prosthesis or implant, and fit the individual with a custom component that is specified to the patient's unique needs (Attaran, 2017). Whit this kind of implants it is possible to reduce surgery time and cost as well as the risk of post-operative complications.

Fig. 2.23: 3D printed human pelvis

The AM is also used in the medical field to realize 3D printed teeth, which are used in dental crowns and bridges. The dental copying ensures low production times along with a durable teeth that can be fitted to the exact specifications of the patient's mouth (Bogue, 2013). Nowadays it is not unexpected to realize 3D parts in a great variety of metals and alloys such as titanium alloys (such as Ti–6Al–4V), Co-Cr alloys, Inconel, stainless steels, aluminium, hard and amorphous metals, copper, niobium and beryllium (Singh & Singh, 2017).

2.5.5 Design philosophies and repairing

In the aerospace field have been developed over the years several design philosophies that have led to an increase in safety standard. The characteristics of the main project philosophies and the ways AM can integrate them are as follows.

Safe life

The safe life philosophy proves that the structural element is not subject to any kind of break during his operational life. Once the life limit is reached, the structural element is replaced, even though it apparently does not show any type of rupture. It is still used for structural elements for which it is impossible to introduce redundancy or for those elements for which any damage (cracks) cannot be detected by inspection before they have already reached critical dimensions.

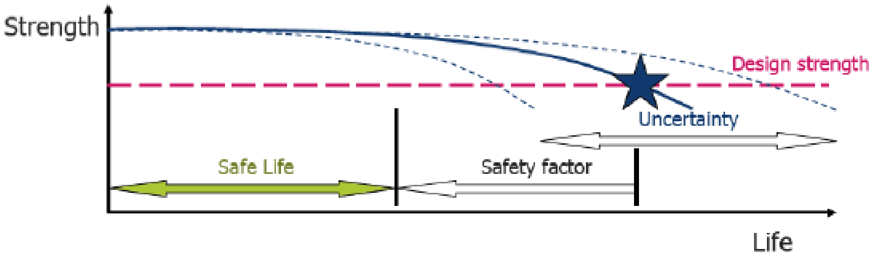

Fig. 2.24: Safe life design philosophy

Fail safe

The aim of this design philosophy is to achieve a structure such that, even if a component is damaged, such rupture does not lead to catastrophic loss of the entire structure. It shall be demonstrated that the residual capacity of the strength of the structure must be able to withstand the applied working load in any case, even in the presence of cracks or breakups. One of the tools used in this philosophy is design redundant: a redundant construction allows to divide lines voltage in multiple load directions.

Damage tolerance

The damage tolerance concept is an evolution of the fail-safe concept. It is assumed that a critical area, previously identified in the project site, contains a crack from the beginning of his life operational. The size of this defect is taken by definition as the greatest value of defect that cannot be seen by the inspection tools in use. A structure is therefore defined as damage tolerant when, even in the presence of a defect due to impact, fatigue or corrosion, its operating life is not altered. The damaged structure can support the loads without a catastrophic break before the defect is identified during maintenance inspections. The purpose of the damage tolerance philosophy for metal structures is to define for each structural element an appropriate timetable of inspections so that cracks (already present or formed later to use) do not propagate until breaking before being identified. This applies to all major structural elements except those so that the manufacturer uses to demonstrate that a damage tolerance approach is not practicable, in which case a safe-life approach is adopted with appropriate scatter factors.

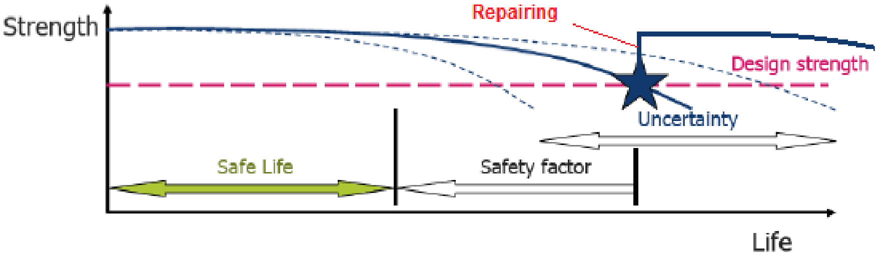

Fig. 2.25: Damage Tolerance design philosophy

The repair of components has a fundamental role in these philosophies, and in the next paragraph, one will be described what Additive Manufacturing role in this framework is and how it proposes itself as an excellent alternative to the conventional repair processes.

2.5.6 Hybrid Additive and Subtractive Manufacturing for repair

Today it is possible to repair parts by using Hybrid LMD-CNC apparatus. In this way, we can extend the components life conceiving a productive chain that considers building new functional components by DED and repair them whit Hybrid DED-CNC equipment if damaged. With this operational philosophy, it is hence possible to repair very costly damaged components instead of replacing them, with a reduction of costs and lead time (R. Liu et al., 2017)

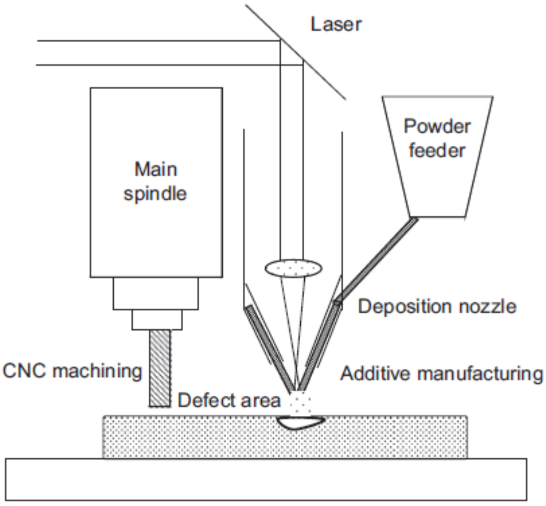

Fig. 2.26: Hybrid AM-CNC apparatus (R. Liu et al., 2017)

Compared to traditional repair methods, such as electron beam, plasma spraying, plasma transferred arc welding and tungsten inert gas welding, these DED based Hybrid machines involve less component distortion and more deposition control with unique simpler equipment (R. Liu et al., 2017). The resulting Heat Affected Zone (HAZ) induced by a DED process is remarkably lower compared to the traditional repairing methods due to the low energy input heat provided by the Additive Manufacturing techniques.

It is possible to divide the repairing process in three steps (R. Liu et al., 2017):

1. Repair preparation stage: the damage is analyzed by camera, laser sensors, and feelers to define the exact measure of the defect and extrapolate its negative area.
2. Manufacturing stage: In this step, you have the material deposition by AM and the subtractive operations.
3. Evaluation stage: an analysis of the allowance and compliance in addition to the fatigue tests and the microstructural characterizations it is taken into account.

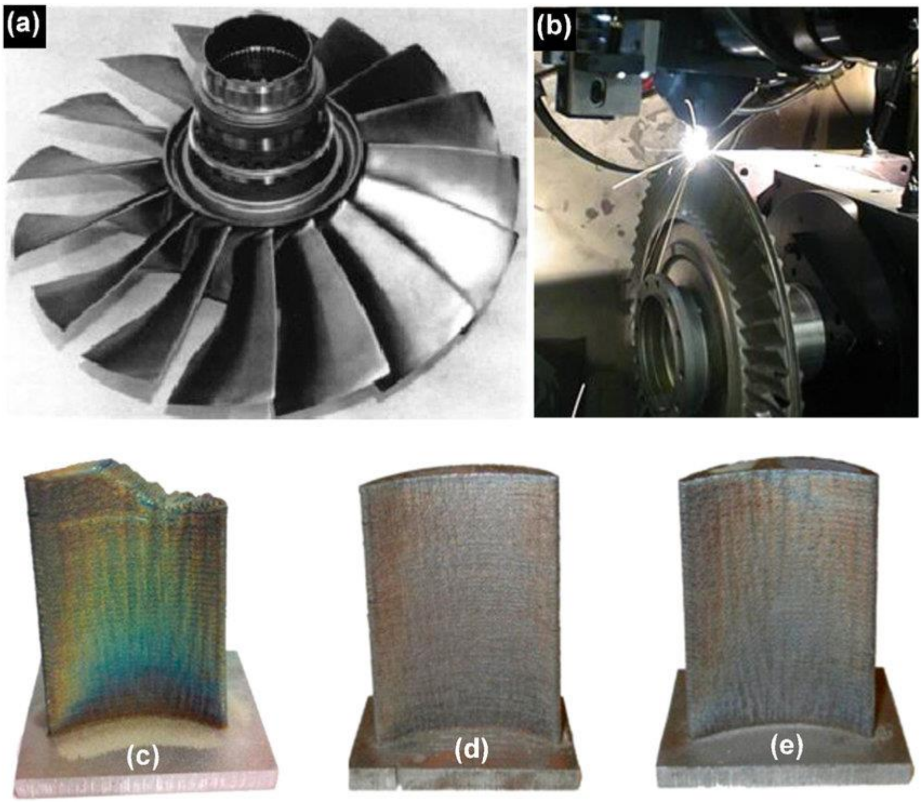

Fig.2.27: Damaged blisk repaired using directed energy deposition process: (a) repaired blisk, (b) repairing in process; damaged turbine blade repaired with directed energy deposition: (c) damaged blade, (d) original undamaged blade, (e) repaired bladed. (S. Liu & Shin, 2019)

Chapter 3

IN 718: microstructure and applications

3.1 Applications

Inconel 718 is a niobium-modified precipitation hardening nickel-iron alloy. It was developed for strength, creep resistance and good fatigue life at high temperatures up to 700 °C (Qi et al., 2009). Thanks to its outstanding strength at elevated temperatures and excellent resistance to fatigue, wear, hot corrosion, oxidation and favourable weldability, it is used in a wide range of high-temperature applications in aircraft, gas turbines, turbocharger rotors, nuclear reactors, liquid-fuelled rockets, and various other corrosive and structural applications. In particular, IN 718 has been used in many aircraft engine components, such as aerofoils, pressure vessel, critical rotating parts and supporting structure reaching more than 30% of the total weight of a modern aircraft engine (Hosseini & Popovich, 2019). The figure below shows the various components of an aircraft engine for which these materials can be used.

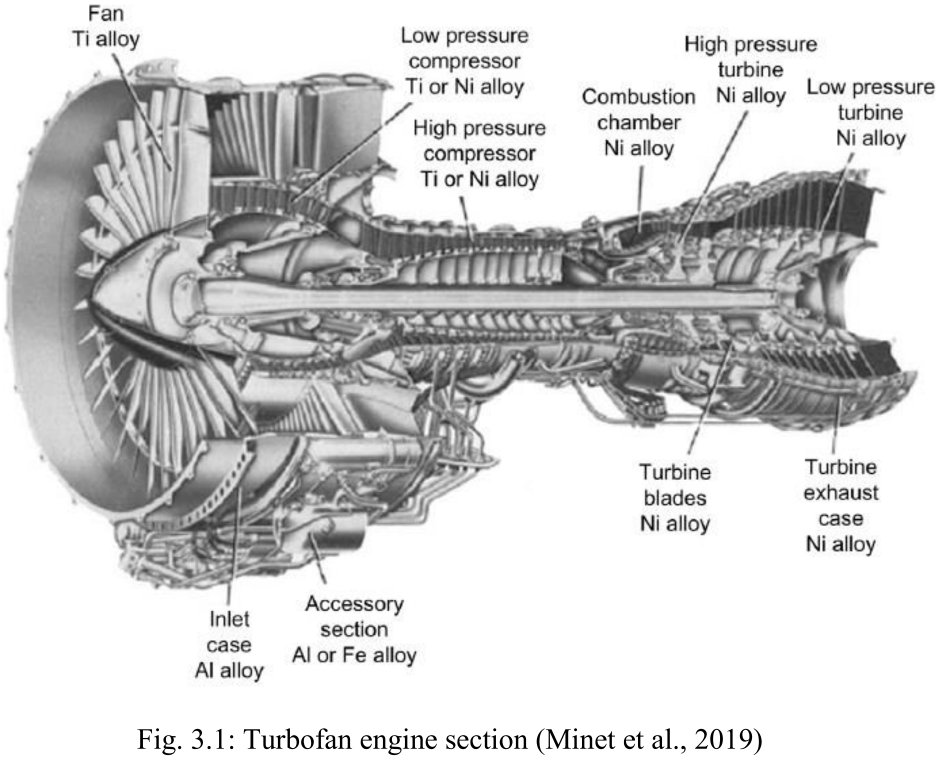

Fig. 3.1: Turbofan engine section (Minet et al., 2019)

The typical composition limits are shown in the table below. As you can see the abundance of varied alloying elements promotes the complex super alloys' microstructure and a great variety of different phases.

Table 3.1: IN718 composition (SLM Technology, 2009)

Element	**Chemical composition [%]**
Nickel (Ni)	50-55
Chromium (Cr)	17-21
Niobium (Nb)	4.75-5.50
Molybdenum (Mo)	2.80-3.30
Titanium (Ti)	0.65-1.15
Aluminium (Al)	0.20-0.80
Cobalt (Co)	≤ 1
Carbon (C)	≤ 0.08
Manganese (Mn)	≤ 0.35
Silicon (Si)	≤ 0.35
Phosphorus (P)	≤ 0.015
Sulphur (S)	≤ 0.015
Copper (Cu)	≤ 0.30

3.2 General microstructure of Nickel-based super-alloys

The most important phases in nickel-based super alloys are as follows (Kulkarni, 2018):

- **Gamma (γ)**: this phase is called Nickel-based austenite and is formed by a continuous matrix with FCC (Face Centered Cubic) crystal structure. The phase is strengthened by solid solution elements such as Co, Cr, Mo, Fe, W, Al and Ti. This phase is the reason why the Nickel-based super alloys exhibits good resistance to high-temperature creep.
- **Gamma Prime (γ')**: this phase is the main one responsible for strengthening and can be obtained by precipitation hardening treatments. The γ' phase is precipitate in the FCC matric of the form A_3B. The electronegative elements such as Ni, Fe and Co are contained in "A" while the electropositive elements such as Al, Nb or Ti are enclosed in "B". The γ' precipitate homogeneously in the matrix due to the low difference in the lattice parameters of γ and γ' (about 0.1%). Usually γ' is $Ni_3(Al, Ti)$.
  The γ' ductile and strengthens the matrix without compromising its fracture toughness. As γ' is long-range ordered, the degree of order increases with increasing temperature which results in high strength in temperature up to 800 °C.
- **Carbides**: Carbon combines with reactive elements such as Ti, Ta, and Hf to form carbides (TiC, TaC, HfC) in a FCC structure. After the heat treatment, the carbides break down to lower order such as $M_{23}C_6$ and M_6C.
  However, carbides may be disadvantageous if their amount exceed a certain percentage (for this reason, the carbon % is limited). Below that percentage, carbides are considered advantageous as they precipitate at grain boundaries, increasing the rupture strength at elevated temperatures.
- **Topologically Close-Packed Phases**: these phases are formed during the heat treatment and are usually undesired because they are mostly brittle and form when the composition of the super-alloy is not properly controlled. These are harmful as they tend to lower the rupture strengths and ductility.

The microstructure of Inconel 718 also contains ordered tetragonal γ'' Ni_3Nb, FCC MX (Nb,Ti)(C,N) in addition to undesired topologically close-packed (TPC) phases, such as hexagonal Laves $(Ni,Fe,Cr)_2(Nb,Mo,Ti)$, orthorhombic δ $Ni_3(Nb,Ti)$ and tetragonal σ CrFe (Hosseini & Popovich, 2019).

Heat treatment processes are generally used to optimize nano-scale precipitation of γ'' and γ' to levels of 16% and 4% respectively (Hosseini & Popovich, 2019).

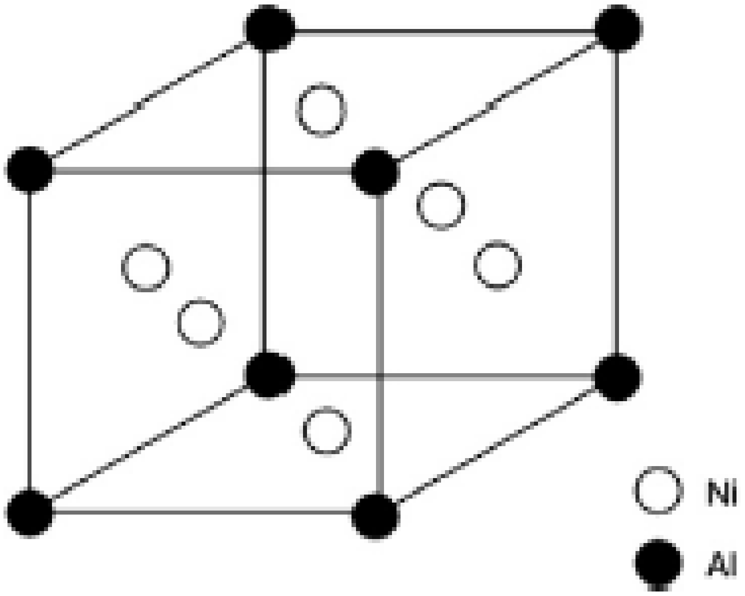

Fig.3.2: γ’- FCC Bravais lattice (Minet et al., 2019)

This super alloys ability to keep their properties at high temperature is due to two strengthening mechanisms (Minet et al., 2019):

- **Strengthening by solid solution of the γ matrix**: due to the wide variety of alloying elements a substitutional solution can occur, which results in some chemical elements replacing the matrix atoms in their lattice positions. Therefore, it generates a strain field interacting and making obstruction during the plastic deformation. Furthermore, an additional strengthening effect is provided if the substitutional elements have a higher Young’s modulus compared to that of the matrix (Goodfellow, 2018).
- **Hardening by precipitation of the γ’ Ni_3(Al, Ti) and the γ’’ Ni_3(Nb) phases**: the dislocations displacement need a higher energy to alter the γ’ precipitates lattice, compared to the γ matrix (Goodfellow, 2018). There are two different shearing dislocations: a “leading” and a “trailing” dislocation. The first interacts with the γ’ lattice: the A1 atoms replace the Ni ones in their lattice positions with an energy increase as an outcome of a bridging zone between the two dislocations (called the Anti-phase region). When the first is passed, the trailing dislocation traverses this region and re-establish the initial lattice order. Otherwise, due to the higher Anti-phase boundary energy (APBE) present in large particles subjected to shear forces, an interaction occurs between the trailing dislocation and the precipitates Anti-phase before that the leading one leaves. This latter phenomenon is defined as “Strong pair coupling” (Goodfellow, 2018).

3.3 IN718 and AM

As seen before, the microstructure of the IN 718 is very complex and miscellaneous due to the many alloying elements present in it. Produce this super alloy by using AM increase the number of parameters related to the microstructure, making it difficult to identify the complete microstructural framework and how the features are related to the process parameters. It seems clear that due to the high cooling rates, temperature gradients and high temperatures during deposition, the resulting microstructure is directly related to the thermal history of the part, which is influenced by process parameters as well as many other factors (Johnson et al., 2017). Furthermore, depending on the parameter set and on the boundary conditions, different microstructural characteristics can be achieved, which are then translated into specific mechanical properties. In fact, the part's mechanical properties vary according to particular grain size, texture, grain type and phases (Akram et al., 2018).

The following sections give an exhaustive summary of reports on the tensile and hardness behaviour of AM Inconel 718 obtained by numerous studies.

3.3.1 Tensile properties

The following figures report the tensile properties for the as-deposited and heat-treated AM Inconel 718. There is a considerable increase of the properties of the alloy after the heat treatment, and that is the main reason of the absence of applications of the as-built material. It can be seen that the ductility and strength of as-built AM IN718 are, respectively, higher and lower than those for the heat treated alloy. This is due to the absence of precipitation hardening from γ' and γ'' phases in the as-built AM alloy (Hosseini & Popovich, 2019). Moreover, the strength values for as-built EBM IN 718 is higher than the SLM ones. The existence of porosity is the main reason for the lower properties of AM IN718 with respect to the wrought alloy.

It may be noted, in the last figure, that the drop in strength for AM IN 718 at high temperatures is marginally more significant than those of the wrought samples.

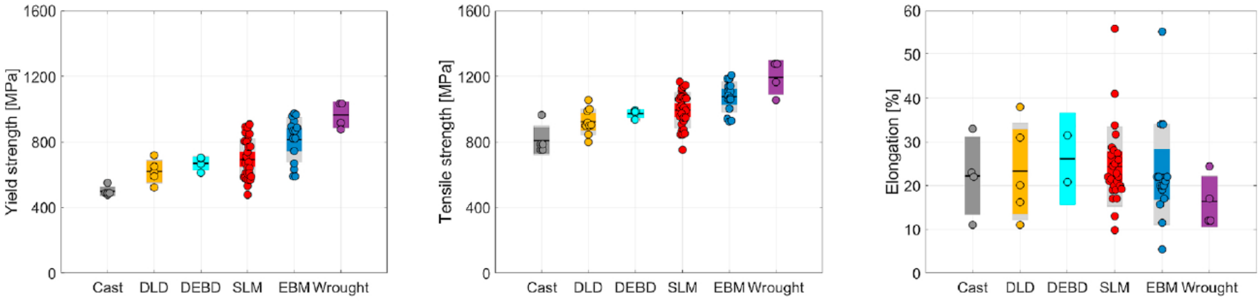

(a) (b) (c)

Fig. 3.3: As-built yield strength, (ultimate) tensile strength and elongation of Inconel 718 manufactured with different MAM processes in comparison with those of the cast and wrought alloys (Hosseini & Popovich, 2019)

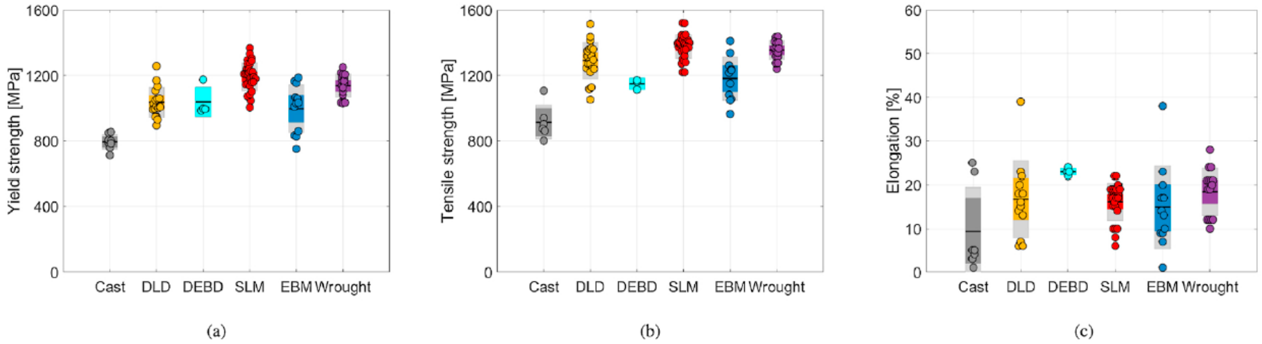

Fig. 3.4: Fully heat treated yield strength, (ultimate) tensile strength and elongation of Inconel 718 manufactured with different MAM processes in comparison with those of the cast and wrought alloys (Hosseini & Popovich, 2019)

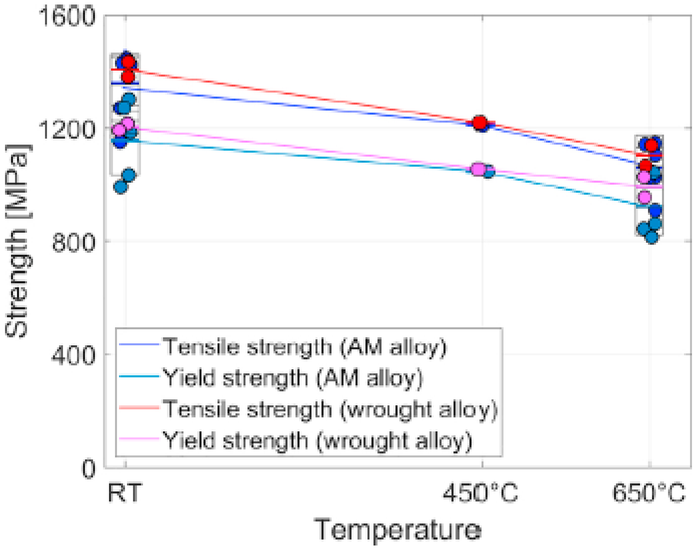

Fig. 3.5: Variation of tensile and yield strengths of heat treated AM and wrought IN718 by temperature (Hosseini & Popovich, 2019)

3.3.2 Hardness

The hardness spatial variation, similar to the observation for the tensile properties, is dependent on the specific MAM technique. Some studies reported that the hardness decreases through the build height: the higher hardness at the bottom of the builds is due to improved precipitation hardening caused by the repetitive heating cycles experienced by the lower region of the builds during the AM process (F. Liu et al., 2013). AM process parameters, such as scanning strategy and input energy, can significantly affect the temperature profile during AM and thus the resulting hardness (Hosseini & Popovich, 2019). The fine structure obtained by rapid heating and cooling transient contributes to the hardness of AM IN 718.

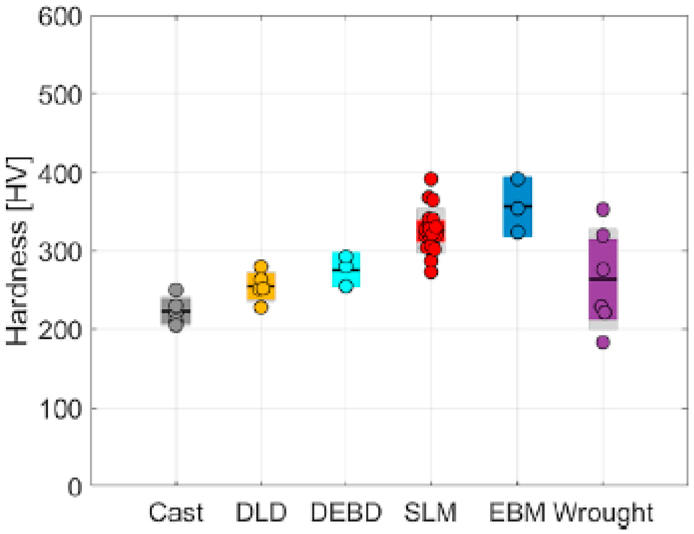

Fig. 3.6: As-built hardness values for IN 718 manufactured with different MAM processes (Hosseini & Popovich, 2019)

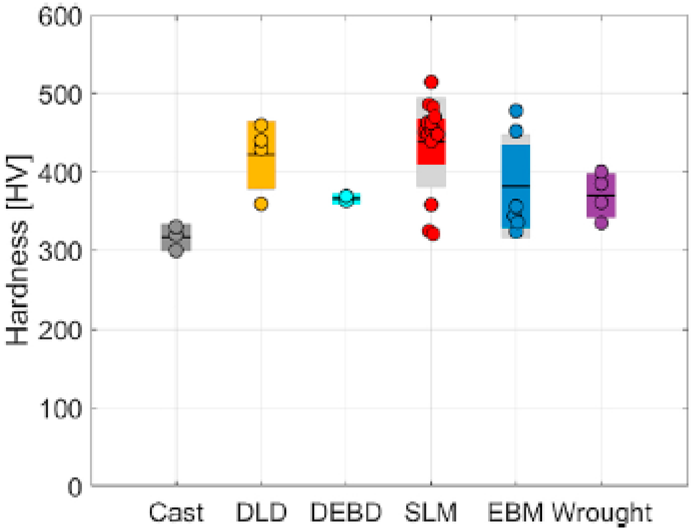

Fig. 3.7: Hardness valued for full heat treated IN 718 manufactured with different MAM processes (Hosseini & Popovich, 2019)

Chapter 4

Material and Methods

For this thesis, have been analyzed three different types of samples:

- 36 “Single Scan Tracks” (SSTs)
- 12 “Single Layers” (SL)
- 2 “Cubes”

These samples have been printed by changing the parameters of:

- Laser Power
- Laser Feed Rate
- Hatching Distance
- Air Blade
- Central Shielding
- Stand off

To evaluate the best combination of parameters.

In this section will be shown the operative procedures used to prepare the specimens for the different characterizations tests, and the equipment employed during the experiment.

4.1 Feedstock material

These samples are realized with gas atomized particles sphere-shaped with an average size ranging between 44 µm and 106 µm. In Table 4.1 are reported the particles chemical composition investigated by EDS.

Tab. 4.1: Powder composition

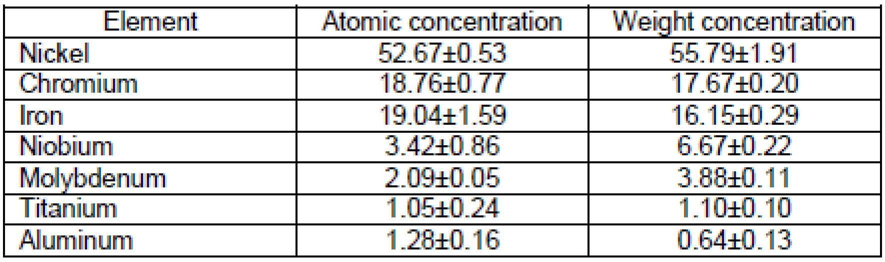

Element	Atomic concentration	Weight concentration
Nickel	52.67±0.53	55.79±1.91
Chromium	18.76±0.77	17.67±0.20
Iron	19.04±1.59	16.15±0.29
Niobium	3.42±0.86	6.67±0.22
Molybdenum	2.09±0.05	3.88±0.11
Titanium	1.05±0.24	1.10±0.10
Aluminum	1.28±0.16	0.64±0.13

4.2 DED Machine

For the printing process have been used a Laser dyne 430 machine supplied by Prima additive. The machine is equipped for closed-loop control by a vision and in-line thermal monitoring and in-process 3D part scan for achieving first time right AM parts (Sciences & Technologies, n.d.).

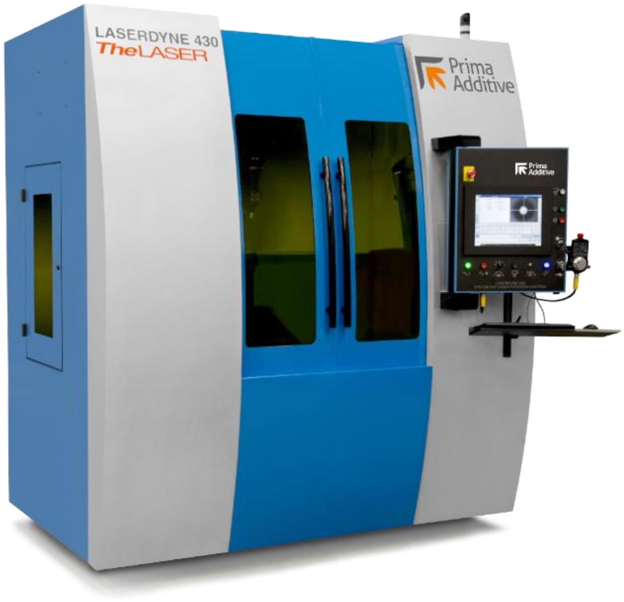

Fig. 4.1: Laserdyne 430 DED machine (*Laserdyne 430* | *Primapower*, n.d.)

4.3 Stereomicroscope

Some images of the SSTs and of the SL have been taken from the top to observing the external surface of the features. For taking those photos, a LEICA EZ4W Stereomicroscope has been used which three magnification of 8x, 10x and 20x.

Fig. 4.2: LEICA EZ4W Stereomicroscope (Control, n.d.)

4.4 Cutting

For the cutting process have been used a Remet TR100s cutting machine, employing a diamond blade driven by a semi-automatic mode, for the initial cuts. Subsequently, for the precision cuts have been used a Presi Mecatome T210, employing a SiC CERMET blade, and a QATM BRILLANT 220 employing a diamond blade.

Fig. 4.3: PRESI MECATOME T210 (on the left) and QATM BRILLANT 220 (on the right) (*Presi Mecatome T210*, n.d.; *QATM Brillant 220*, n.d.)

4.5 Sampling

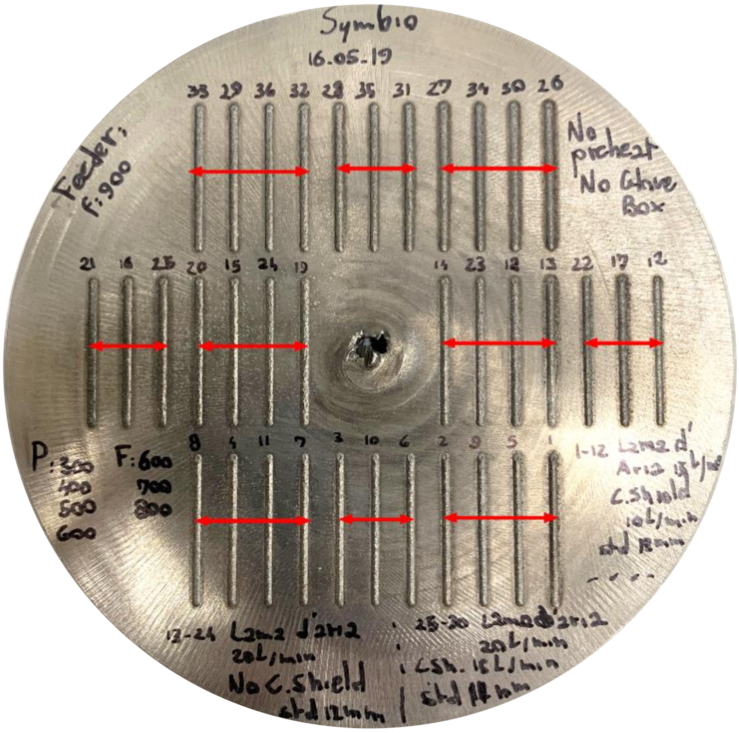

Fig. 4.4: SSTs sampling

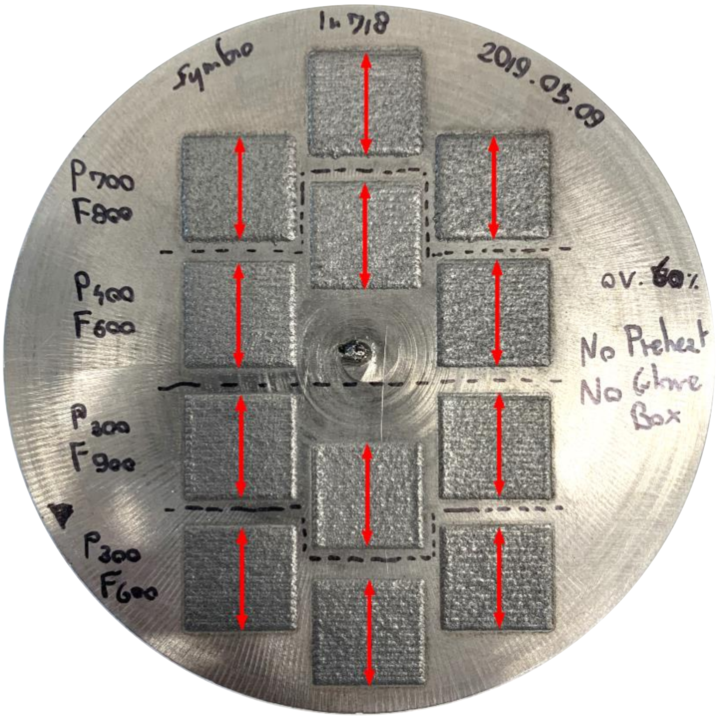

Fig. 4.5: SL sampling

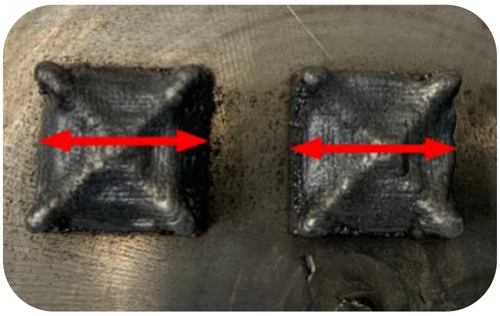

Fig. 4.6: Cubes sampling

4.6 Mounting

After the cutting operations, the ten SSTs samples and the twelve SL have been mounted using a Remet IPA 30 mounting machine. This operation is necessary in order to make easier to handle the samples and to safeguard the edge of the feature's cross-section during the polishing operations.

Fig. 4.7: Remet IPA 30 mounting machine (*Remet IPA 30*, n.d.)

4.7 Grinding and Polishing

For the polishing operations have been used a Presi Mecatech 234 polishing machine reaching a final value of around 1μm. For reaching this target roughness, we used a set of abrasive cards respectively of #FEPA:

- 320
- 500
- 800
- 1000
- 2500

After this step, we used two pads bearing a mixture of diamond particles of 3 μm and 1 μm with a lubricant alcohol-based solution.

Fig. 4.8: PRESI Mecatech 234 (*Presi Mecatech 234*, n.d.)

4.8 Chemical etching

The samples have been chemically etched with the Kalling's No.2, a metallographic etchant, to see clearly the microstructure. Kalling's composition is as follows:

- $CuCl_2$ 5 gr
- Ethanol absolute 100 ml
- Hydrochloric acid 100 ml

The samples have been immersed for 20-25 seconds, then cleaned with distilled water and dried with compressed airflow.

4.9 Optical Microscope

For the analyzing operations, before and after the etching process, we used a LEICA DMI 5000. The samples have been analyzed at 50x and 100x.

Fig. 4.9: LEICA DMI 5000 (*Leica DMI5000M*, n.d.)

Chapter 5

Results and Discussion

5.1 Purposes

The purpose of this experimental campaign is to identify the optimal process parameters concerning the manufacturing of IN 718 components produced by DED technology.

The analyzed features have been realized by SUPSI and are part of the EU project 4D Hybrid, the purpose of which is to develop a new concept of hybrid AM and to demonstrate the effective application to aerospace, oil & gas, and power generation sectors.

These features have been deposited on IN 718 not pre-heated substrates to recreate the repairing operation. The features coherence with the substrate and their compliancy with functional applications was the focus of the analysis process.

5.1.1 Features specification and themes of analysis

The SSTs have been printed employing:

- 4 Laser Power levels (P) [W]: 300, 400, 500, 600
- 3 Feed Rate levels (F) [mm/min]: 600, 700, 800
- 2 Air blade levels [l/min]: 15, 20
- 2 Central Shielding levels [l/min]: 0, 10
- 2 Stand-off values: 11, 12

And characterized in:

- Track morphology
- Heat Affected Zone (HAZ) width
- Melt Pool morphology and regularity
- Coherence with the substrate

The best sets of process parameters were determined after the analysis process by choosing the ones that generally provide an optimal deposition.

The SLs have been printed employing:

- 3 Laser Power levels (P) [W]: 300, 400, 700
- 3 Feed Rate levels (F) [mm/min]: 600, 800, 900
- 4 hatching distance levels (HD) [mm]: 0.468, 0.536, 0.556, 0.568

And characterized in;

- Regularity
- Porosity/oxides percentage area
- Etched morphology

The Cubes have been printed employing the same parameters for all three features:

- Laser Power Level (P) [W]: 300
- Feed Rate (F) [mm/min]: 900
- Hatching distance (HD) [mm]: 0.468
- Layer Thickness [mm]: 0.202
- Air Blade level [l/min]: 20
- Central Shielding level [l/min]: 10

And characterized in:

- Porosity/Oxides percentage area
- Microstructure

The obtained results are reported in the final chapter to define the best parameters needed for an optimum DED process.

5.2 Single Scan Tracks characterization

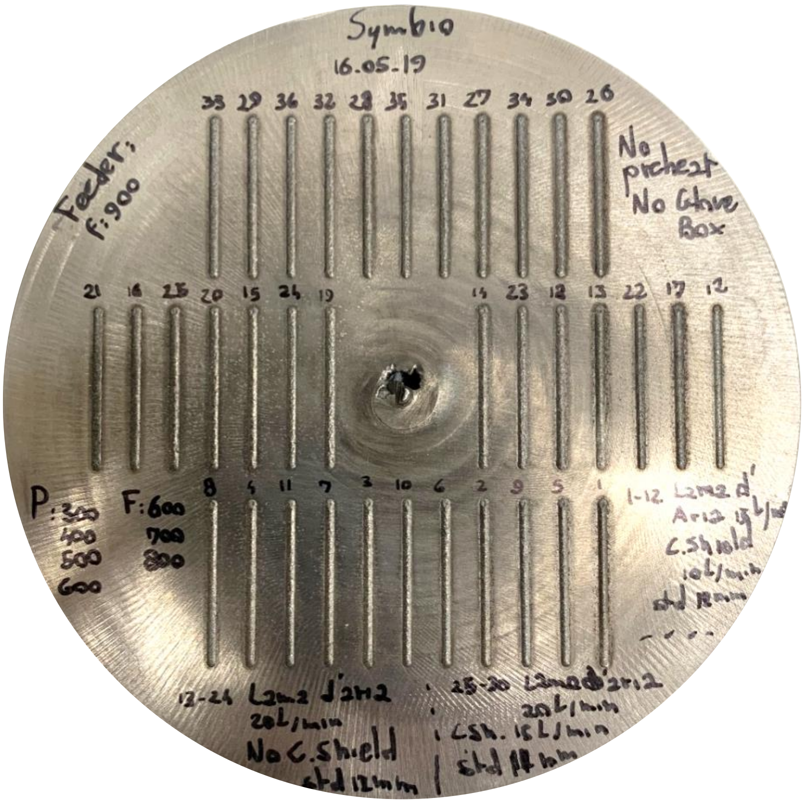

Fig. 5.1: Single Scan Tracks

Tab. 5.1: SSTs indexing

	FEED RATE [mm/min]								
LASER POWER [W]	**600**			**700**			**800**		
600	1	13	25	2	14	26	3	15	27
500	4	16	28	5	17	29	6	18	30
400	7	19	31	8	20	32	9	21	33
300	10	22	34	11	23	35	12	24	36

5.2.1 Single Scan Tracks morphology

In the following figure are collected the images took with the LEICA stereomicroscope at a magnification of 10x. In this way, it is possible to obtain a first distinction focused on detecting tracks that present unacceptable defectology of deposition.

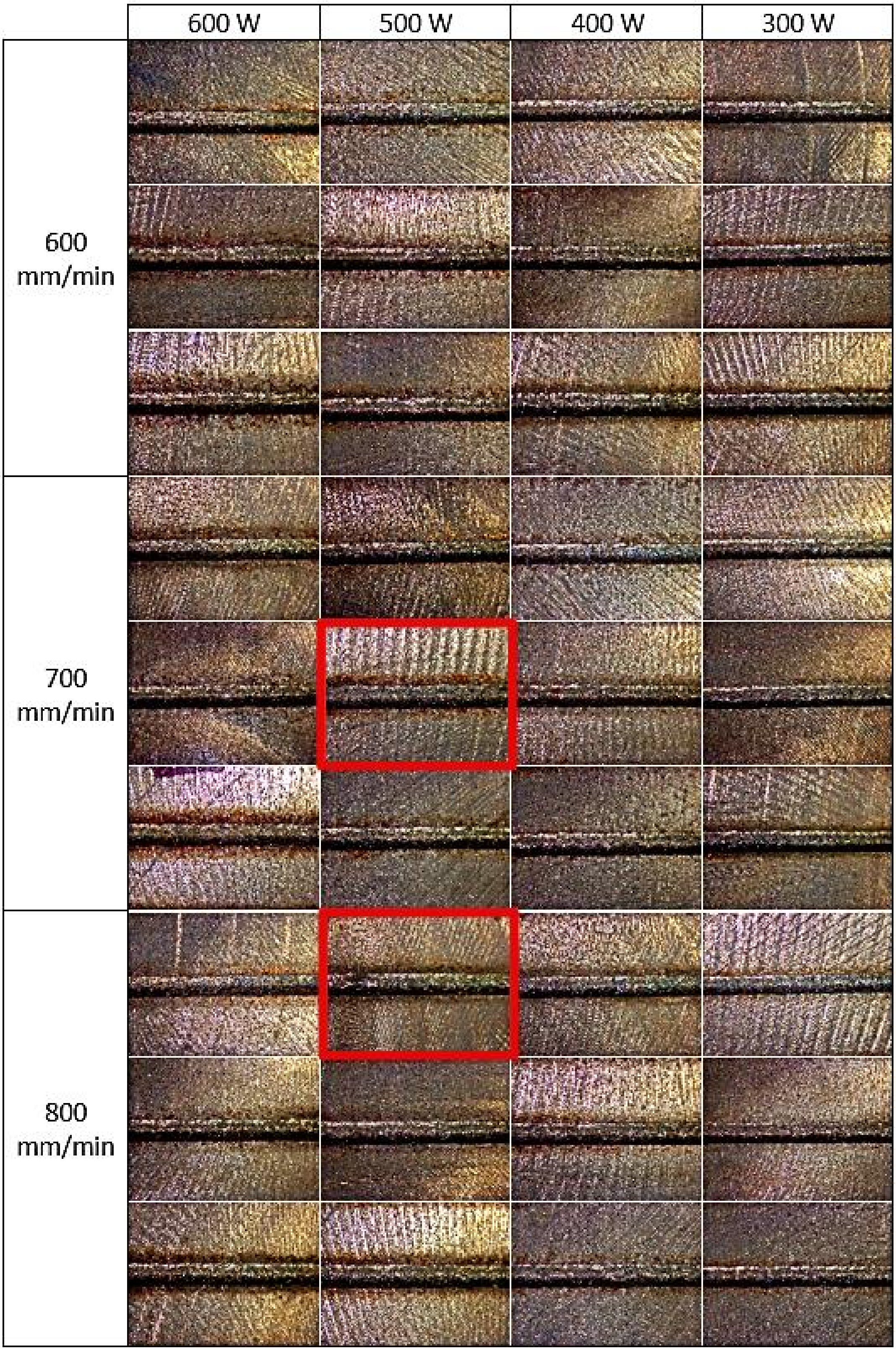

Fig. 5.2: SSTs "On top" analysis at 10x magnification

All the SSTs seems stable except for the SST:

- 6 (P=500 W and F=800 mm/min)
- 17 (P=500 W and F=700 mm/min)

However, the defectology detected in SST 6 could be likely caused by an instability of the deposition head, such as an unexpected acceleration, or by a sudden drop in the powder flow.

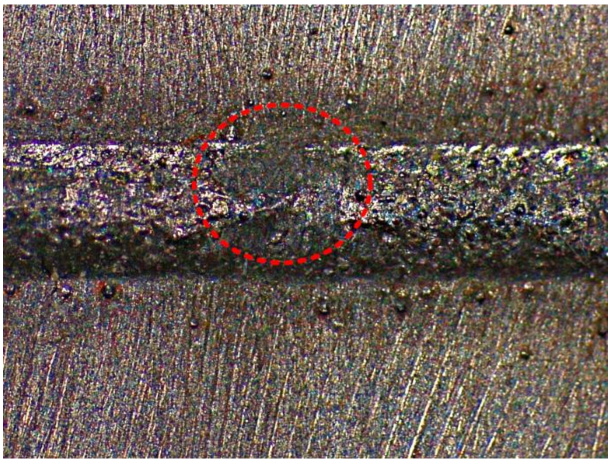

Fig. 5.3: SST 6 at 20x magnification

Instead, the non-linearity of the SST 17 should not been associate to a problem of the parameter used, because the other SST printed with the same parameters present an acceptable deposition profile linearity. For this reason, the non-linearity of the SST 17 can be the result of some problem with the deposition head.

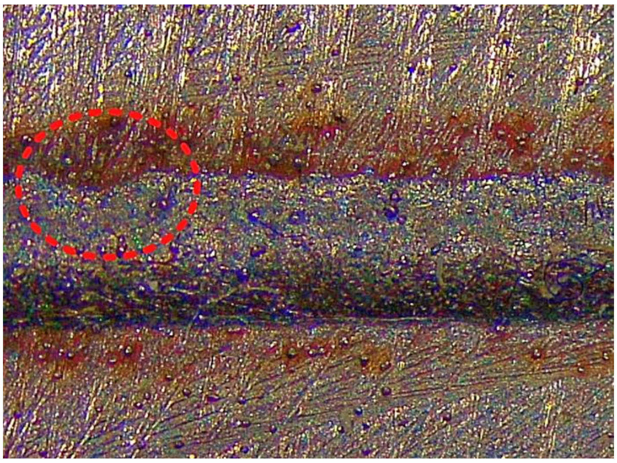

Fig. 5.4: SST 17 at 20x magnification

This is the reason why we could not exclude some of the couples of parameters and should continue with the analyses of the HAZ and of the Melt Pools.

5.2.2 SSTs and Heat Affected Zone (HAZ) regularity

In this section, we are going to analyze deeper the interaction between the as-deposited material and the substrate by taking into account the HAZ as seen by the On Top images. The HAZ, such as the coherency with the substrate, is a fundamental parameter in view of a use in terms of repair.

Therefore, have been taken further images of the SSTs at a magnification of 10x and 20x. The HAZ width has been measure, by using the software “ImageJ”, six times at the magnification of 10x and six times at 20x, for a total of twelve measures. Then the Arithmetic Mean “A” and the Standard Deviation “SD” were calculated, and their trends plotted in relation to the Feed Rate and the Laser Power levels of the SSTs.

Tab. 5.2 HAZ “A” and “SD” values at different Feed Rate and Laser Power levels

	Laser Power							
	600 W		500 W		400 W		300 W	
Feed Rate	A [µm]	SD [µm]	A [µm]	SD [µm]	A [µm]	SD [µm]	A [µm]	SD [µm]
600 mm/min	478.667	92.933	593.433	38.494	576.483	60.610	426.733	38.576
	574.304	52.538	518.633	66.774	302.233	66.766	425.150	30.519
	671.716	76.795	477.833	57.249	480.400	53.7895	380.467	60.597
700 mm/min	576.783	54.911	545.366	48.590	509.066	17.522	485.133	60.351
	470.316	40.516	524.000	69.781	419.283	39.965	328.283	81.967
	682.333	68.601	446.200	60.284	332.050	45.161	322.300	40.942
800 mm/min	582.783	42.269	545.033	36.544	455.250	50.309	341.300	41.688
	441.350	77.048	495.217	58.204	441.283	47.063	311.3895	50.238
	558.846	63.961	489.050	85.120	393.417	48.417	317.100	60.562

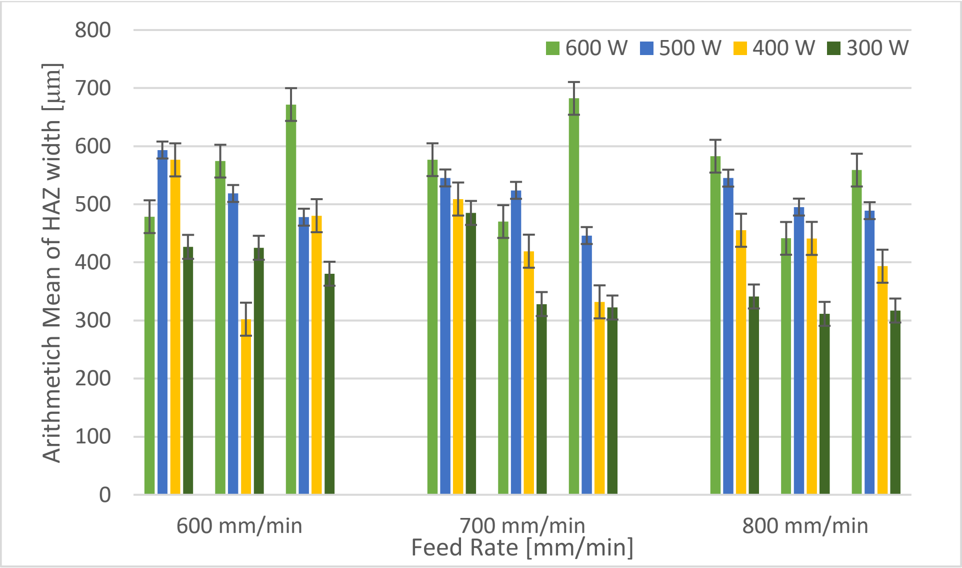

Fig. 5.5: HAZ “A” and Standard Deviation “SD” at different Feed Rate and Laser Power levels

In the following chart are represented the mean values of the width of the HAZs to better understand the trend for each couple of parameters.

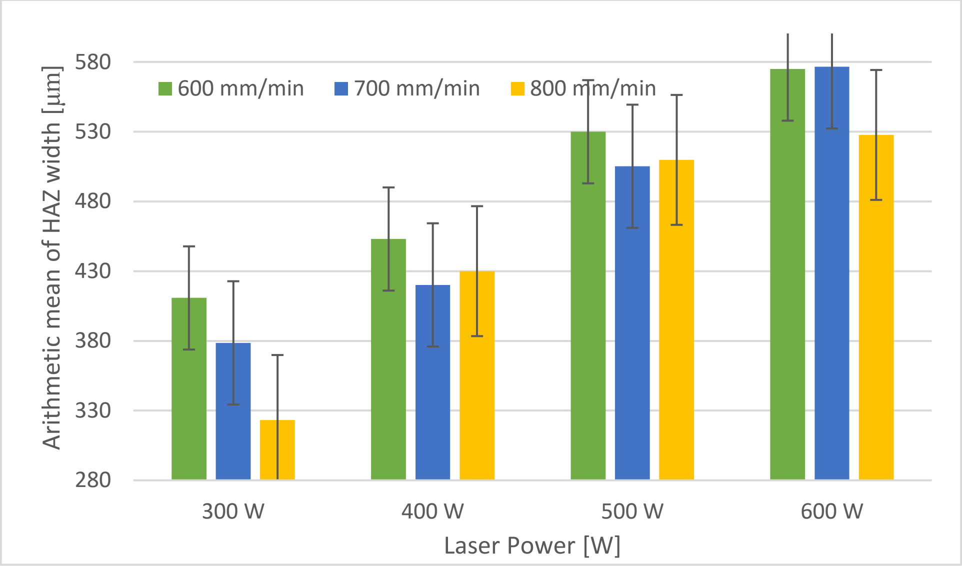

Fig. 5.6: Mean values of HAZ "A" at different Feed Rate and Laser Power levels

In overall, the HAZ Arithmetic Mean width increases, at a parity of feed rate levels, as the laser power level increases.

Instead, the trend at a parity of laser power is hardest to define except for the 300W SSTs in which we could see that a higher feed rate level involves a lower arithmetic mean of HAZ width. In Fig 5.5 can be noticed some incongruences with this theory and the following SSTs shows HAZ widths lower than expected:

- 1 (P=600 W; F=600 mm/min)
- 14 (P=600 W; F=700 mm/min)
- 15 (P=600 W; F=800 mm/min)
- 19 (P=400 W; F=600 mm/min)
- 28 (P=500 W; F=600 mm/min)

From this data, it was possible to recognize a general dependency of the HAZ's width values with the Feed Rate and the Laser Power levels:

- Higher Laser Power levels involve a higher HAZ's width
- Higher Feed Rate levels involve a lower HAZ's width

5.2.3 SSTs etched Melt Pools HAZ

In repair operations, the HAZ plays a fundamental role because it cannot be considered expendable material since it is a functional component. For this reason, the HAZ should be as less pronounced as possible to avoid, in a macroscale perspective, remarkable microstructural inhomogeneity because of the repeated layers of annealing.

Therefore, have been taken some images of the SSTs cross-sections after the polishing operation with the optical microscope at a magnification of 50x to detect the presence of cracks and porosity within the melt pools.

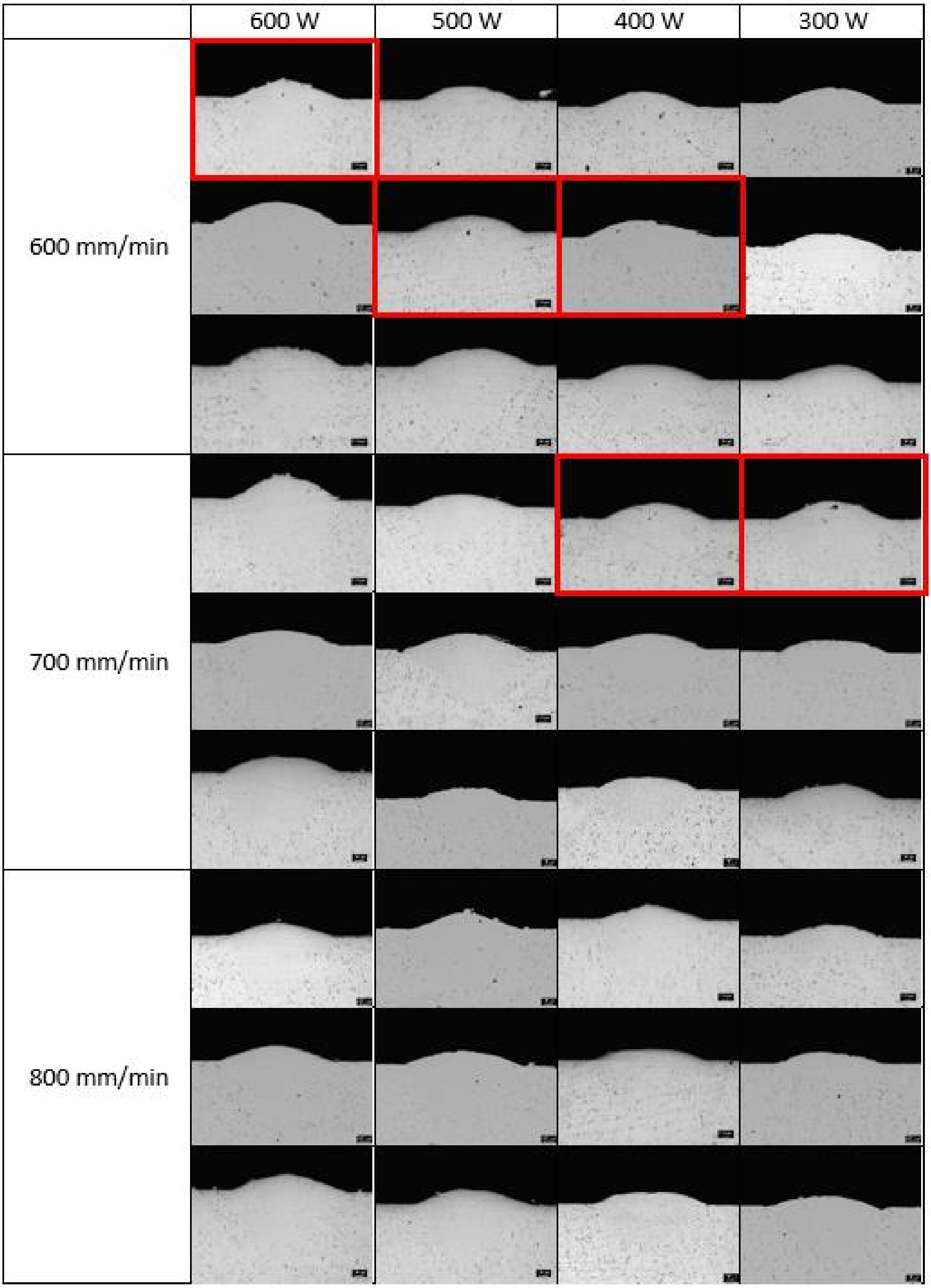

Fig. 5.7: SSTs melt polls at 50x magnification: red outlined whether porosity detected

As seen in the previous image, no defected was detected in the melt pool or in the substrate and consequently the SSTs have been etched and the inner HAZs measured. The cracking in the HAZ is usually for the alloys with a combined amount of Al and Ti that exceeds 6 wt%, due to the rapid precipitation of the γ’ phase during the welding process that creates high stress levels (Li et al., 2018).

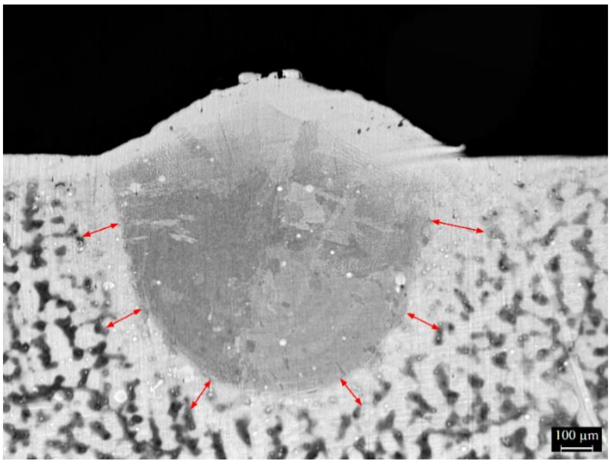

Fig. 5.8: SST n° 2 inner HAZ at 50x magnification

For measuring the inner HAZs have been taken six measure on an OM image at a 50x magnification and then the mean values have been plotted with HAZ's "On top" values.

It is possible to notice a huge difference between the "On top" values and the inner values. A smaller HAZ in the melt pool should reduce the areas overlaying the deposition layer metallurgically altered with an increase of the mechanical properties and a more homogenous structure.

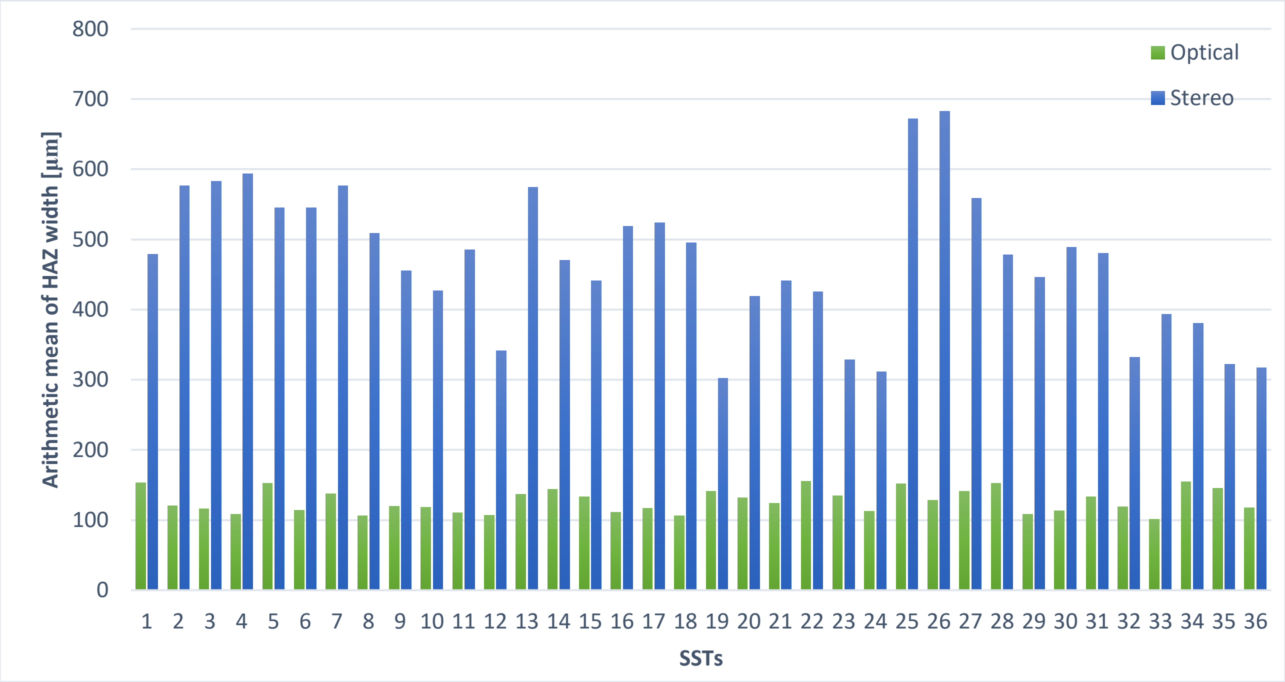

Fig. 5.9: HAZ comparison

5.2.4 SSTs etched Melt Pools Morphology

In the first analysis of the melt pool morphology, a-symmetry criterion was taken into account, as previously done for the "On top" analysis. This geometrical aspect at first defines the effectiveness of the process parameters employed because a symmetric Melt Pool leads to a deposition coherence with the substrate along its dimensions. Moreover, a melt pool asymmetry can generate interposed porosities and a lack of fusion between the further overlapped tracks.

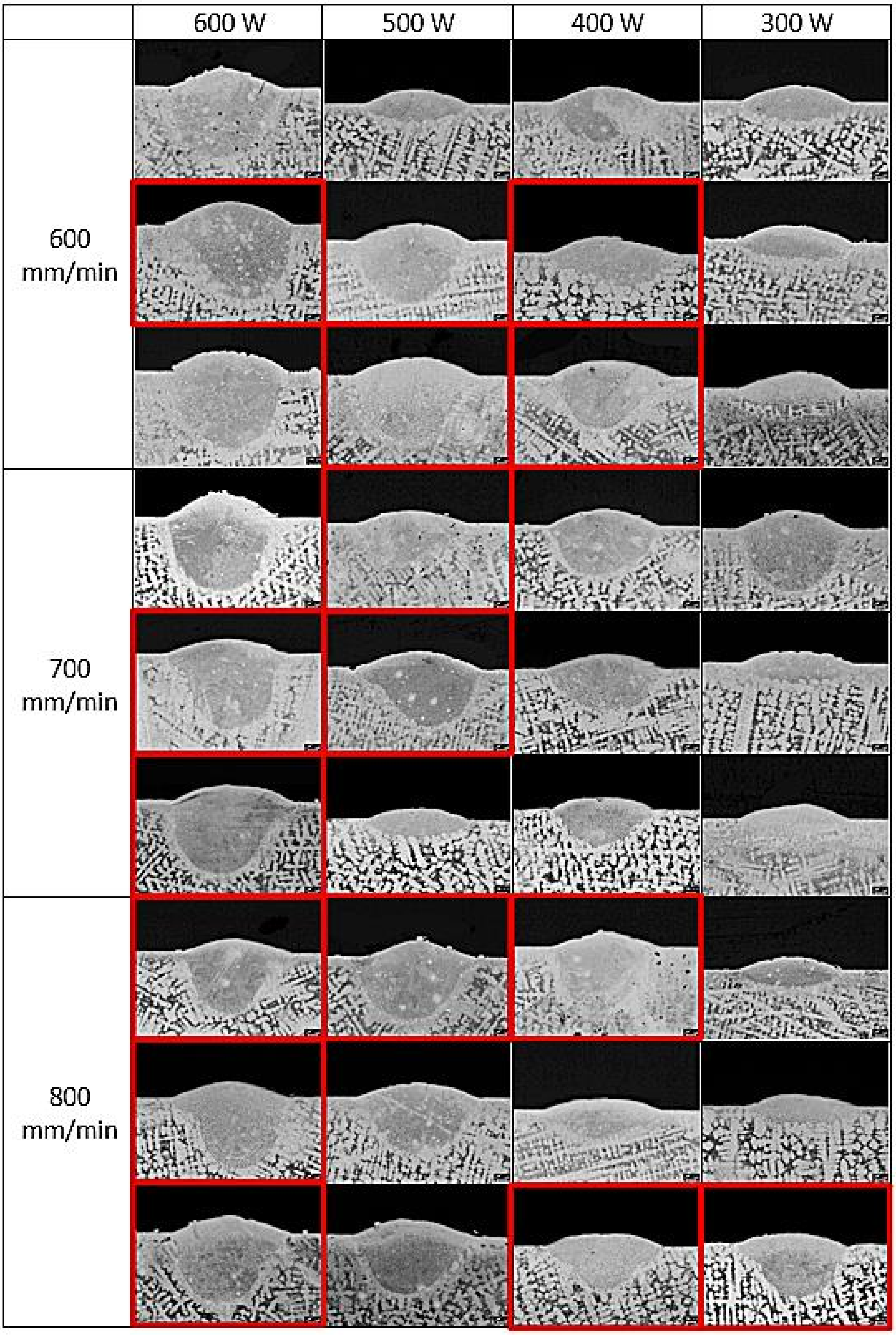

Fig. 5.10: SSTs etched melt pools at 50x magnification acquired with an optical microscope: red outlined whether asymmetric melt pool

According to the previous assumptions, a lack of symmetry has been detected at high Feed Rate level (800 mm/min) and at a high Laser Power level (600 W). The SSTs with an asymmetric melt pool are red outline and are the following:

- 3 (P= 600W; F= 800mm/min)

- 5 (P= 500W; F= 700mm/min)
- 6 (P= 500W; F= 800mm/min)
- 9 (P= 400W; F= 800mm/min)
- 13 (P= 600W; F= 600mm/min)
- 14 (P= 600W; F= 700mm/min)
- 15 (P= 600W; F= 800mm/min)
- 17 (P= 500W; F= 700mm/min)
- 19 (P= 400W; F= 600mm/min)
- 26 (P= 600W; F= 700mm/min)
- 27 (P= 600W; F= 800mm/min)
- 28 (P= 500W; F= 600mm/min)
- 31 (P= 400W; F= 600mm/min)
- 33 (P= 400W; F= 800mm/min)
- 36 (P= 300W; F= 800mm/min)

5.2.5 SSTs Melt Pool's width, Fusion depth and Bead height

After the etching, it is possible to recognize the melt pool's main features: "Melt Pool Width", "Bead Height" and "Fusion Depth" (Fig. 5.11). Starting from the etched melt pool's images acquired at a 50x magnification (reported in Fig. 5.10), the features have been measured by using the software ImageJ. From the data collected (shown in the following charts and table), it is possible to state that the "Bead Height" decreases at fixed laser power level as the feed rate level increase, while the "Melt Pool's Width" and the "Fusion Depth" had a remarkable increment when the laser power level increases at constant feed rate. These three general trends find confirmation in literature as reported by (Chen & Mazumder, 2017; Mahamood & Akinlabi, 2018; Thompson et al., 2015). However, to better understand the relationship between these three parameters, they have been deeply analyzed and compared.

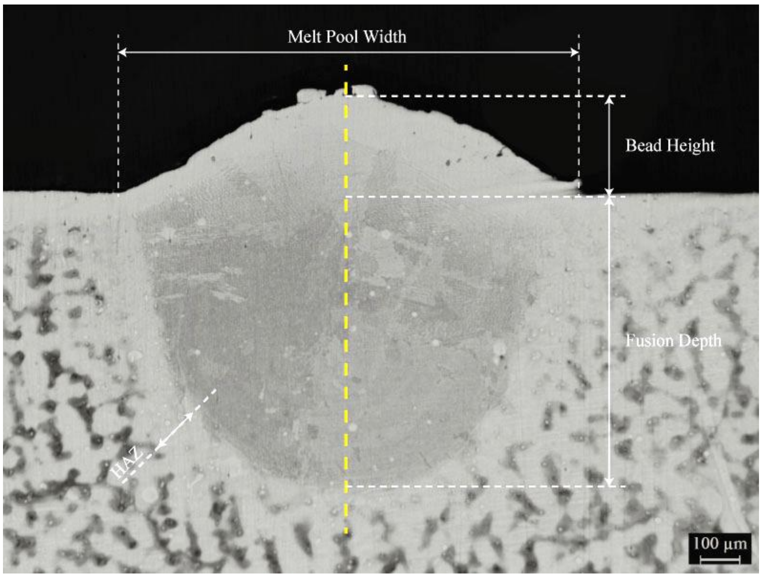

Fig. 5.11: Melt Pool's width, Bead Height, Fusion Depth at 50x magnification

5.2.5.1 Melt Pool's width

Generally, the melt pool's width increases with the laser power rising (Fig. 5.13), nevertheless some SSTs have been found that conflict with this trend:

- 3 (600 W; 800 mm/min)

- 4 (500 W; 600 mm/min)
- 8 (400 W; 700 mm/min)
- 15 (600 W; 800 mm/min)
- 16 (500 W; 600 mm/min)
- 27 (600 W; 800 mm/min)
- 32 (400 W; 700 mm/min)

This samples show a melt pool's width lower than that of the samples printed with the same Feed Rate level and a lower Laser Power level. To understand the reason of these discrepancies, the 16th and the 19th (400W; 600 mm/min) have been selected.

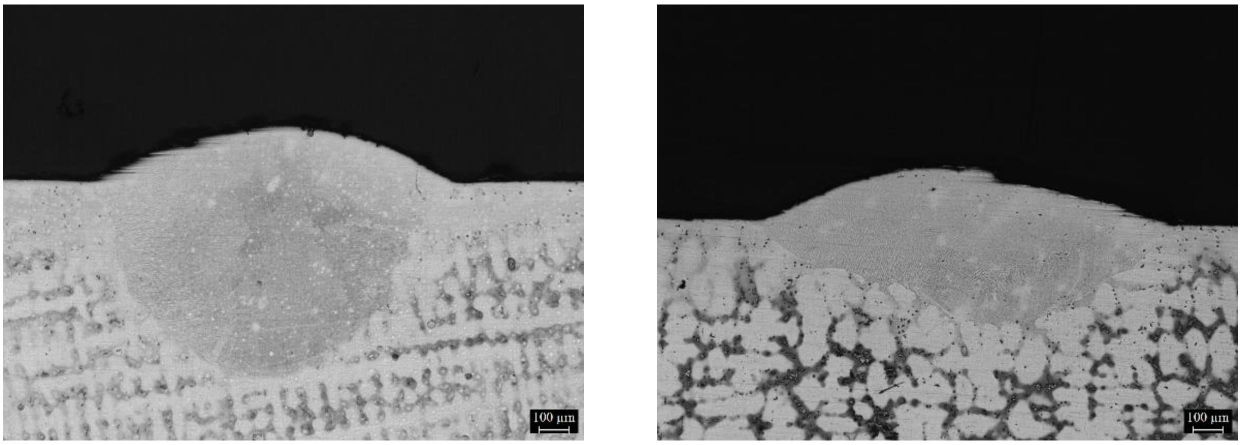

Fig. 5.12: SST 16 on the left and SST 19 on the right at 50x magnification

The SST 19 own a higher melt pool's width than the SST 16 of about 150 µm, even though created with a lower P. On the other side, the SSTs 16 presents a higher Fusion Depth zone (about 290 µm), thanks to a higher P adopted. This behaviour (lower melt pool's width and higher fusion depth compared to a SST with the same F and lower P) have also been recognized in the SSTs 3, 15, 27 and 32. At the same time, the SSTs 4 and 8 present lower melt pool's width and fusion depth compare to SST with the same F and lower P.

This trend could find an explanation in the heat transfer modes rising inside the Dynamic Melt Pool during the deposition process (Thompson et al., 2015). The heat generated during the printing process inside the material is transferred to the substrate by a conductive and a convective manner. In these SSTs, the convective heat transfer mode is the prominent one and creates a convective flow with a predominant z-axis component due to the high laser power levels. As a consequence of the direction high specific energy used, the melt pool has a Fusion Depth more marked compared to the melt pool's width.

The "Width/Fusion Depth" is another fundamental parameter evaluated. At the ideal value of "1" the melt pool's geometry results to be round-shaped with good interaction with the substrate. From the chart reported in Fig 5.14 it is possible to see that the parameter decreases with an increase of laser power P. However, as we can see by the data reported, these ideal values has never been reached due to an insufficient laser power level P.

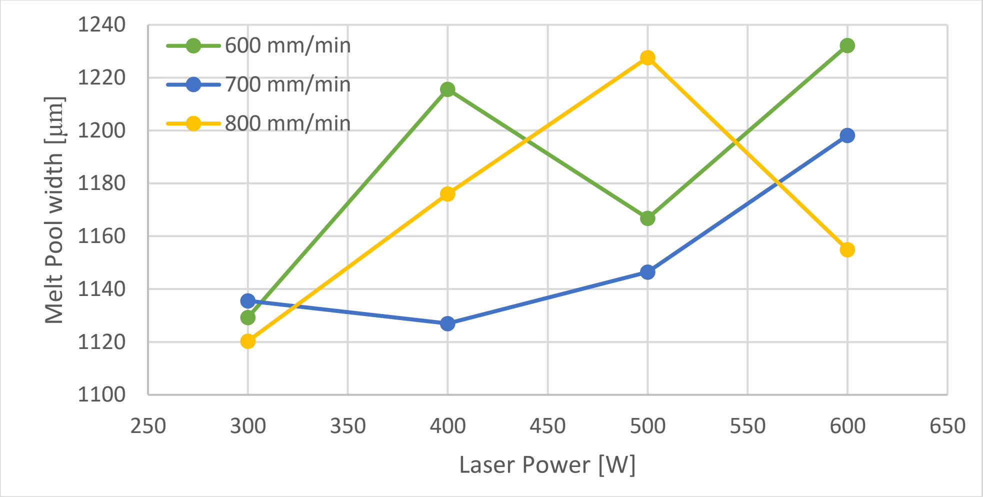

Fig. 5.13: SSTs Melt Pool's width at different Feed Rate and Laser Power levels

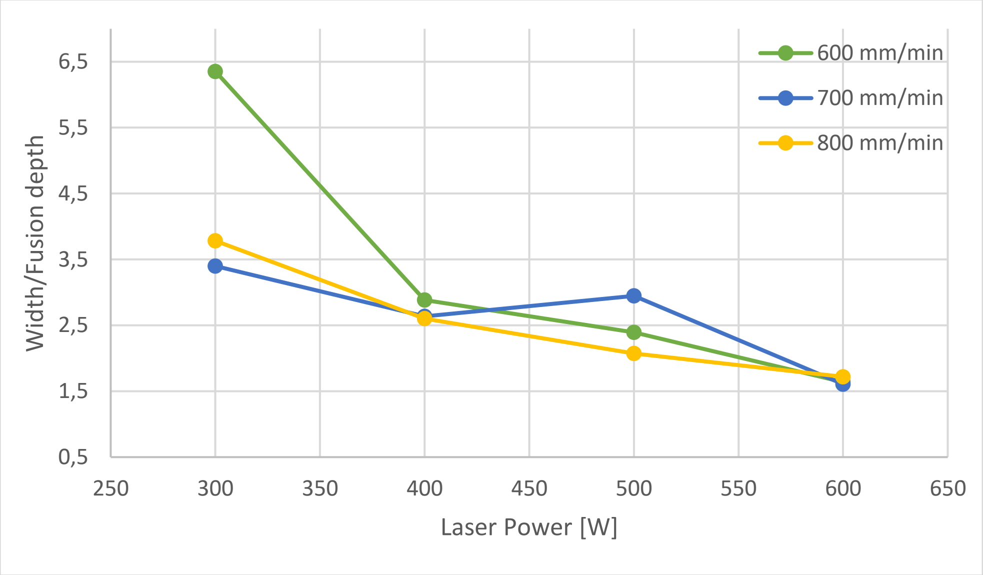

Fig. 5.14: SSTs Width/Fusion Depth at different Feed Rate and Laser Power levels

5.2.5.2 Melt Pool's Bead Height

The generic trend, for this parameter, consist of a Bead Height increase at fixed Feed Rate with the Laser Power rising while decreases at fixed Laser Power with the Feed Rate rising. However, some SSTs have been found in conflict with this trend:

- 5 (P=500 W; F=700 mm/min);
- 29 (P=500 W; F=700 mm/min);
- 32 (P=400 W; F=700 mm/min);

The SSTs "5" and "29" presents a lower Bead Height compared to the SSTs at higher Feed Rate and same Laser Power levels, while the SST 32 Bead Height decreases compared to the SSTs at lower Laser Power and same Feed Rate levels.

The "Width/Bead Height" ratio is shown in Fig 5.17 at different Laser Power and Feed Rate levels. This ratio should tend to "one" to obtain a bead Height perfectly balanced with the melt pool's width and a good side and transversal overlapping between the tracks. This ratio decreases at high laser power level and low feed rate. However, in this experiment have been reached the lowest value of about “5.5” suggesting a remarkable deviancy from the ideal value.

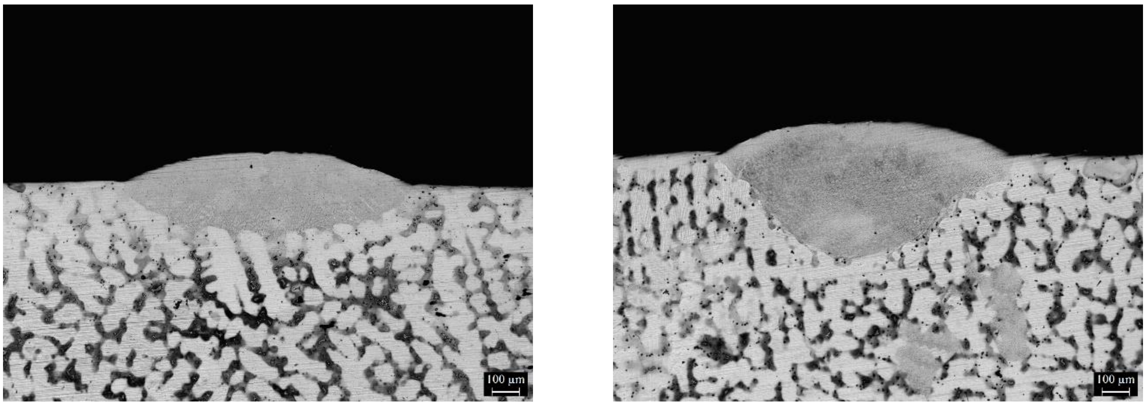

Fig. 5.15: SST 29 (on the left) and SST 32 (on the right) at 50x magnification

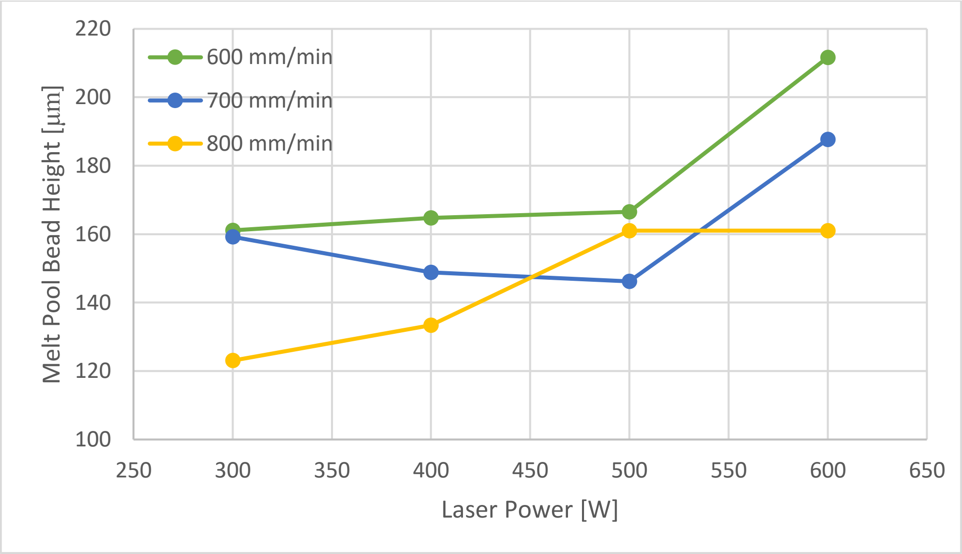

Fig. 5.16: SSTs Melt Pool’s Bead height at different Feed Rate and Laser Power levels

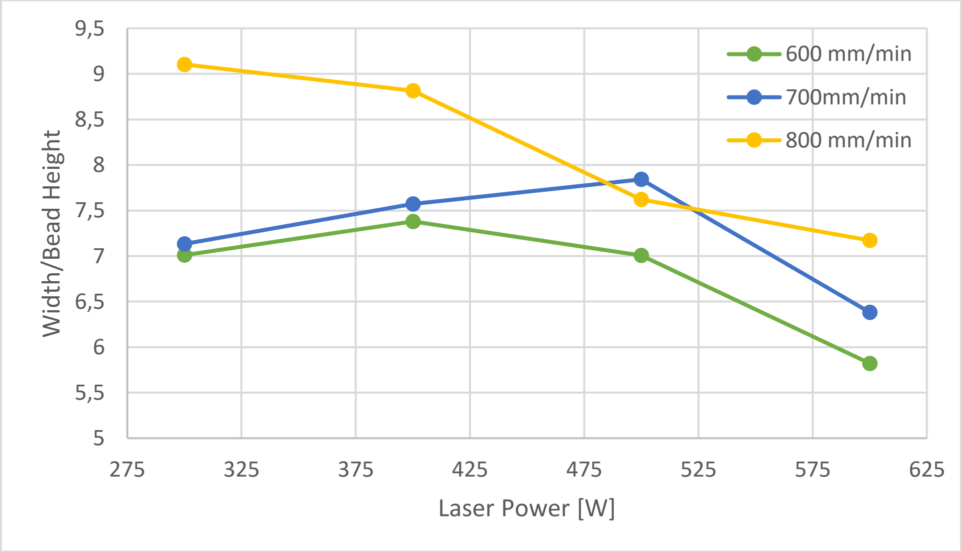

Fig. 5.17: SSTs Width/Bead Height at different Feed Rate and Laser Power levels

5.2.5.3 Fusion Depth

The general trend for the Fusion Depth, as shown in the Fig 5.18, consist of an increase at fixed Feed Rate with the Laser Power rising. However, the SSTs “5” and “29” (P=500 W; F=700 mm/min) are in contradiction with this trend. They present a lower Fusion Depth in comparison with the SSTs performed with the same Feed Rate and lower Laser Power levels.

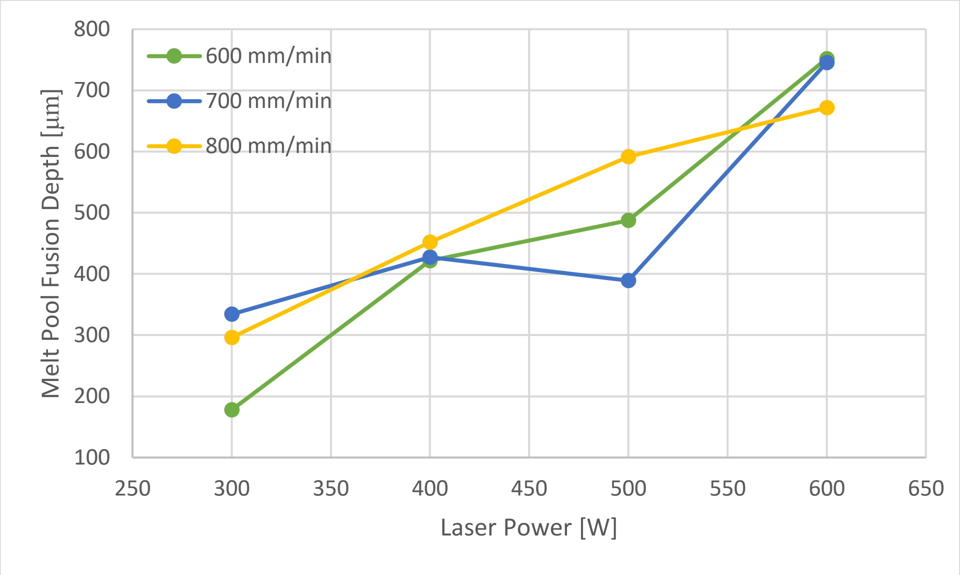

Fig. 5.18: SSTs Melt Pool’s fusion depth at different Feed Rate and Laser Power levels

Tab. 5.3: SSTs Width, Bead Height and Fusion Depth

Laser Power [W]	Feed Rate [mm/min]	Melt Pool Width [µm]	Bead Height [µm]	Fusion Depth [µm]
600	600	1167.821	193.252	712.270
		1292.025	226.38	761.963
		1236.81	215.337	781.288
	700	1142.958	245.706	745.399
		1223.006	149.080	759.202
		1228.528	168.405	731.595
	800	1096.012	140.798	610.123
		1178.834	165.644	701.227
		1189.877	176.687	703.988
500	600	1049.080	140.798	176.687
		1187.117	182.209	629.448
		1264.417	176.687	657.055
	700	1126.384	138.037	397.546
		1292.025	193.252	568.712
		1021.101	107.339	200.917
	800	1181.624	171.166	615.644
		1247.853	151.840	571.472
		1253.374	160.123	588.037
400	600	1107.055	160.123	394.785
		1336.196	171.166	342.331
		1203.681	162.883	527.301
	700	1118.098	168.405	507.975
		1217.485	162.883	408.589
		1045.427	115.244	364.939
	800	1126.380	154.601	634.969
		1209.202	118.712	303.681
		1192.374	126.994	416.871
300	600	1104.294	162.883	196.012
		1154.463	146.553	166.012
		1129.141	173.926	171.166
	700	1173.313	201.534	612.883
		1112.577	118.712	207.055
		1120.859	157.362	182.209
	800	1054.601	126.994	168.405
		1145.706	118.712	184.969
		1160.671	123.476	535.061

5.3 Single Layers characterization

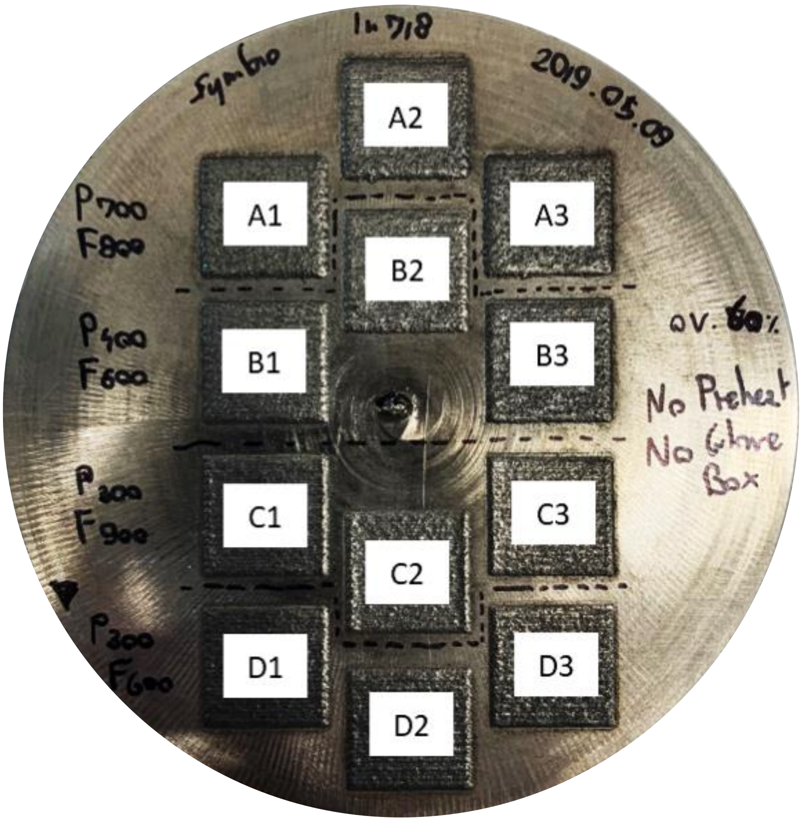

Fig. 5.19: Single Layers

Tab. 5.4: Printing parameters

Layer Number	Power [W]	Feed Rate [mm/min]	Hatching Distance [mm]
A	700	800	0.536
B	400	600	0.568
C	300	900	0.468
D	300	600	0.556

For these samples have been used three different Laser Power levels (300 W; 400 W; 700 W), three different Feed Rate levels (600 mm/min; 800 mm/min; 900 mm/min) and four Hatching distance (0.468 mm; 0.536 mm; 0.556 mm; 0.568 mm). Each set of parameters have been printed three times.

5.3.1 Single Layer “On Top” analysis

The images taken with the LEICA stereomicroscope at 8x and 20x have been reported in the following figure. Starting from the “On Top” images, it is possible to detect eventual deposition defects that occurred during the printing process. None of the Single Layers presents some sort of defect or incongruence with the substrate.

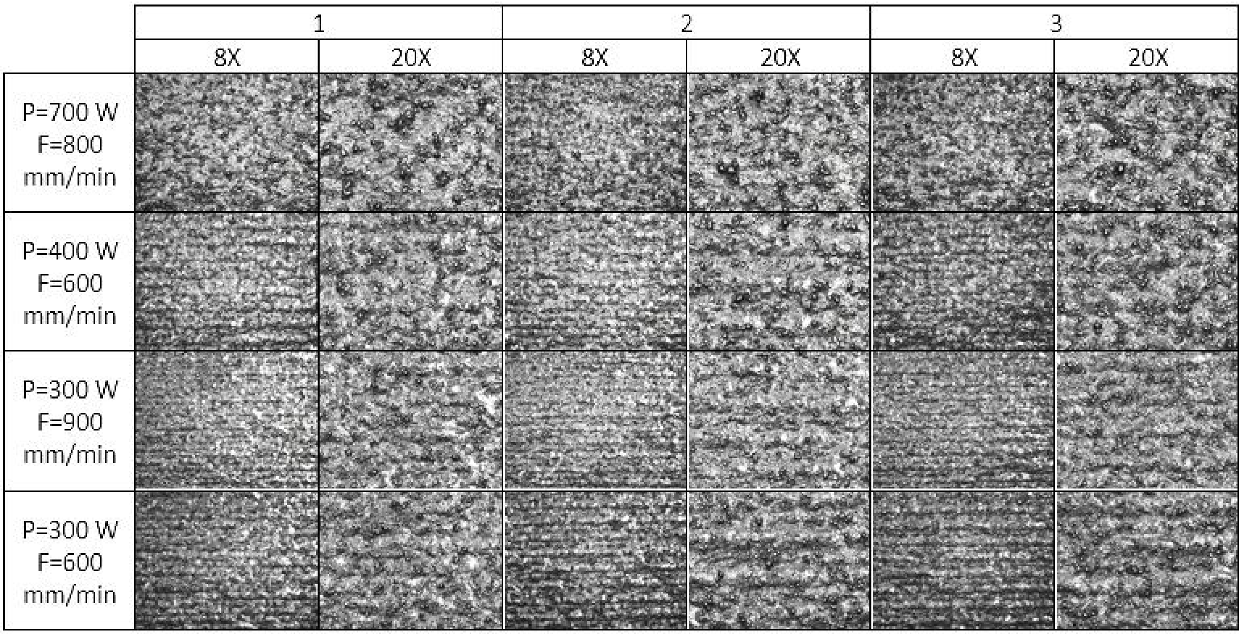

Fig. 5.20: SL “On Top” images at 8x and 20x magnification

5.3.2 SL Inclusions and Porosity analysis

The layers have been optically observed after the polishing process in their cross-section at a 50x magnification and analyzed in order to detect the presence of defect and inclusions.

By observing the cross-section of an IN 718 samples can be detected two types of defects: porosity and oxides. These two kinds of defects cannot be clearly distinguished one from each other and for this reason. They are considered as a unique feature. It is important to specify that porosity and oxides have a negative effect on the final performance and must be minimized.

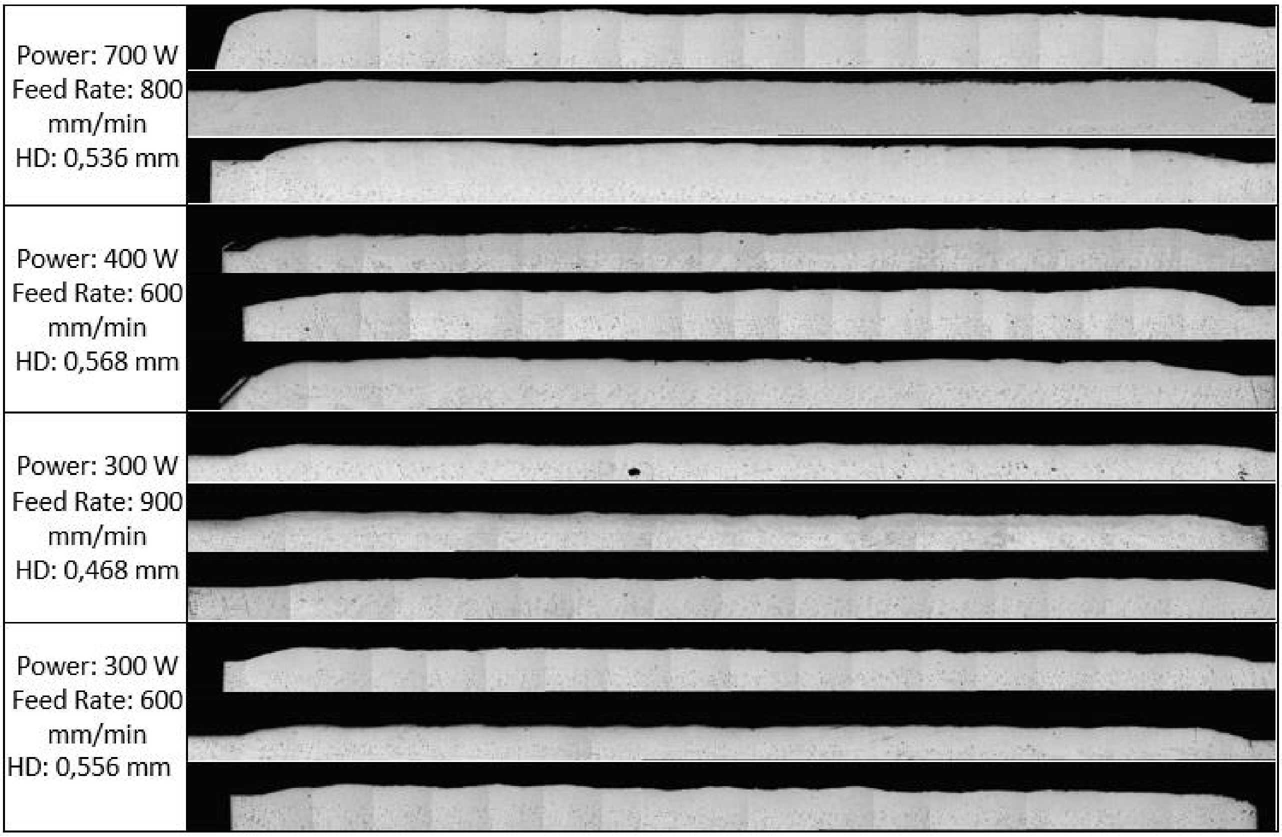

Fig. 5.21: SLs at 50x magnification after the polishing operation

Each samples have been photographed around 20 times to cover the entire length and to obtain the images reported in Fig. 5.21. Then they have been analyzed with the "ImageJ" software by isolating the defects from the background through the use of a minimum detection size of 2 μm and a minimum circularity of 0.5.

From the obtained results seems clear that the most relevant defects are in the layers of the "A" family (P=700 W; F=800 mm/min; HD=0.536 mm) with a mean percentage area value of 0.084%. On the other hand, the "D" family (P=300 W; F=600 mm/min; HD=0.556 mm) presents the lowest mean percentage area (0.037%).

According to the experimental data seems that lower Laser Power and Feed Rate levels leads to a lower defects percentage area, while for the Hatching Distance trends does not look so clear.

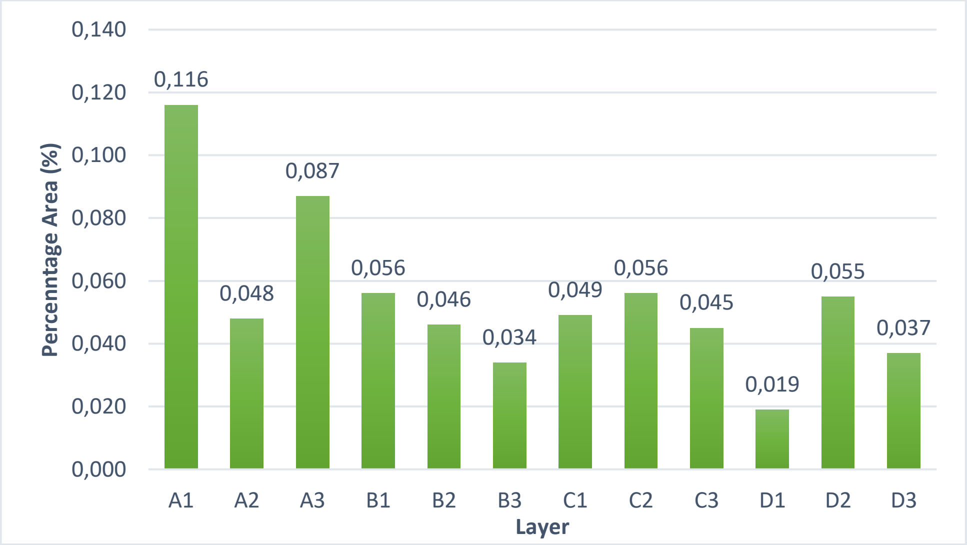

Fig. 5.22: SLs Percentage Area

As we can see from the data reported in Fig 5.23, the "C" family (P=300 W; F=900 mm/min; HD=0.468 mm) presents the lowest average size mean values with 10.802 µm. Instead, as well as for the percentage area, the "A" family (P=700 W; F=800 mm/min; HD=0.536 mm) obtains the highest values of 16.212 µm.

As noticed for the percentage area, the lowest values of average size are obtained with the lowest Laser Power and Hatching distance level. However, a high Feed Rate level and a low Hatching distance provide a low porosity average size.

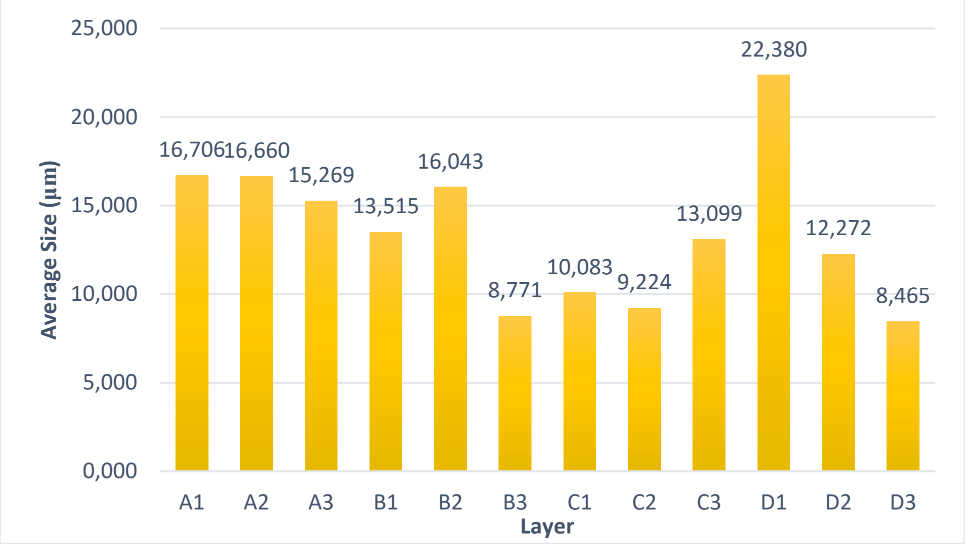

Fig. 5.23: SLs Average Size

5.3.3 Etched Single Layers morphology

Subsequently, the single layers have been etched with the Kalling's No.2 for 20 seconds in order to see clearly the melt pool structure and the interaction between the deposited material and the substrate.

As done before after the polishing operations, each layer has been photographed to cover the entire length.

The resulting images are reported in Fig. 5.24.

Fig. 5.24: Etched SLs at 50x magnification

The layers were compared in their morphology by valuating, as previously done for the Single Scan track, “Melt Pool’s width”, “Fusion Depth” and “Bead Height” in order to understand what set of parameters ensures the most homogeneous deposition and the best coherence with the substrate.

To evaluate the Bead Height and the Fusion Depth have been taken five measures with a 50x magnification for each layer, while for the Melt Pool’s width the total length of the layer have been divided for the melt pool’s number. The obtained results are summarized in the following table.

Tab. 5.5: SL Melt Pool’s width, Bead Height and Fusion Depth

Layers number	Power [W]	Feed Rate [mm/min]	Melt Pool's Width [µm]	Bead Height [µm]	Fusion Depth [µm]
A1	700	800	557.825	324.786	782.839
A2			586.183	361.863	745.456
A3			578.705	373.276	714.825
B1	400	600	537.057	295.129	271.671
B2			563.111	318.184	215.825
B3			581.720	336.889	155.265
C1	300	900	568.676	220.957	124.804
C2			570.334	198.199	177.629
C3			568.186	205.524	169.559
D1	300	600	558.344	267.533	165.210
D2			580.388	264.304	185.729
D3			554.536	275.283	170.352

According to this experimental data, it is possible to say that the Laser power and the Feed Rate levels do not influence the Melt Pool's width. On the other side, these two parameters highly influences the Bead Height and the Fusion Depth. A higher Laser Power level involves a remarkable increase in the Fusion Depth while has a minor influence on the Bead Height value.

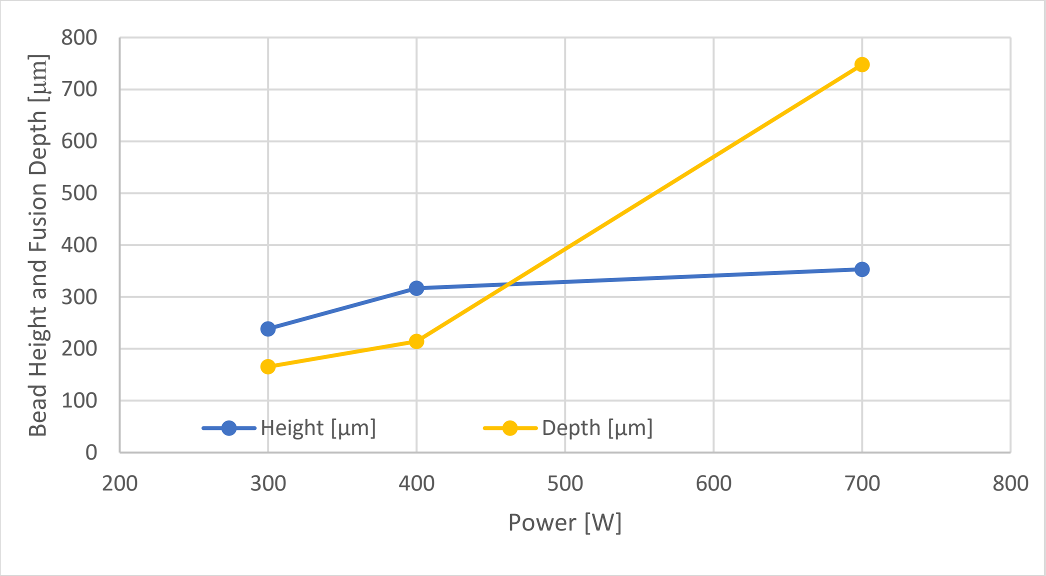

Fig. 5.25: SLs Melt Pool's width, Bead Height and Fusion Depth at different Laser Power levels

The trend as a function of the Feed Rate is not so clear. It is possible to notice optimum values, of both the features, with a Feed Rate level of 800 mm/min and an important decrease at higher Feed rate as shown in the following figure.

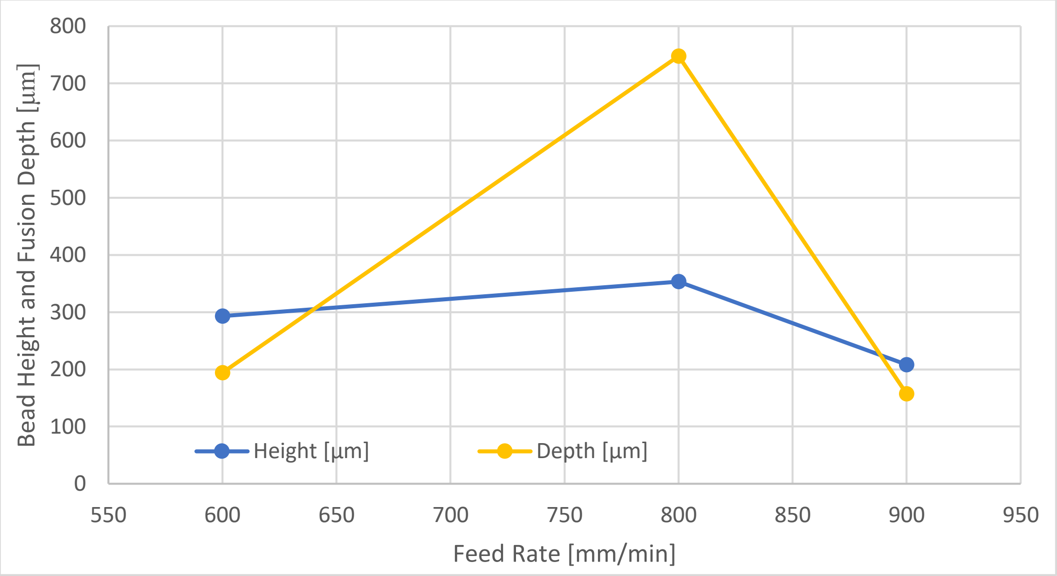

Fig. 5.26: SLs Melt Pool's width, Bead Height and Fusion Depth at different Feed Rate levels

From the data collected from the previous analysis seems clear that a higher Laser Power level provides better morphological values in addition to good substrate coherence. However, as a consequence of the high Laser Power level, the Single layers presents a high defect average size and percentage area values that could result in a reduction of the tensile and mechanical properties.

The Bead Height obtained at 700 W is remarkable higher than the ones obtained at lower laser power levels and could increase the repairing rate.

5.4 Bulks/Cubes Characterization

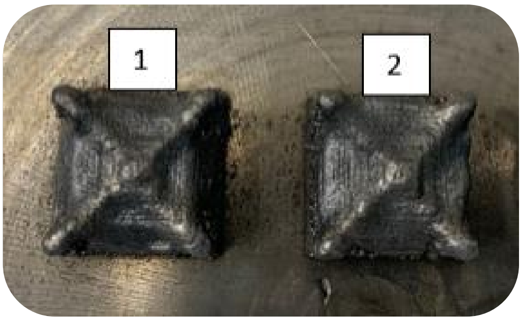

Fig. 5.27: Cubes

Tab. 5.6: Cubes parameters

	Feed Rate [mm/min]		
	900		
Laser Power [W]	Hatching Distance [mm]		
	0.468		
300	1	2	3

5.4.1 Defect analysis of the Cubes

As previously done for the SLs analysis, we started with an optical inspection at 50x magnification after the polishing operations. The goal was to identify potential defect and inclusions.

Even if this inspection method presents several limits, it is good for preliminary analysis and allowed to calculate the porosity of the Cubes and to verify the eventual presence of defects. As reported in the following charts, the average defect size is slightly higher than the one calculated for the Single Layers while the mean values of the percentage area is almost ten times higher than the previous one.

These Cubes presents a higher Percentage Area and Average Size if compared with the Single Layers printed with the same parameters, the "C" family (P=300 W; F=900 mm/min). However, it is important to remember that this analysis is indicative because the porosity morphology is not distinguishable from that of oxides.

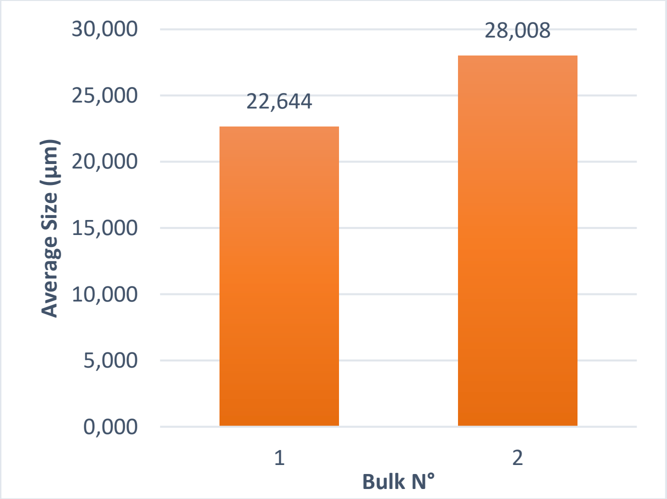

Fig. 5.28: Bulk's porosity average size

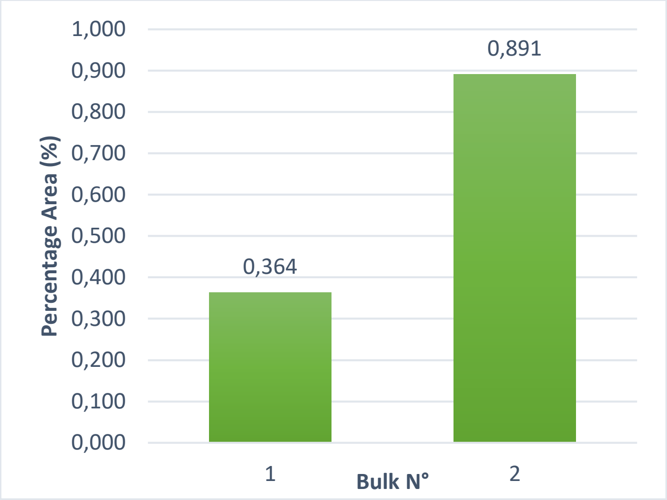

Fig. 5.29: Bulk’s porosity percentage area

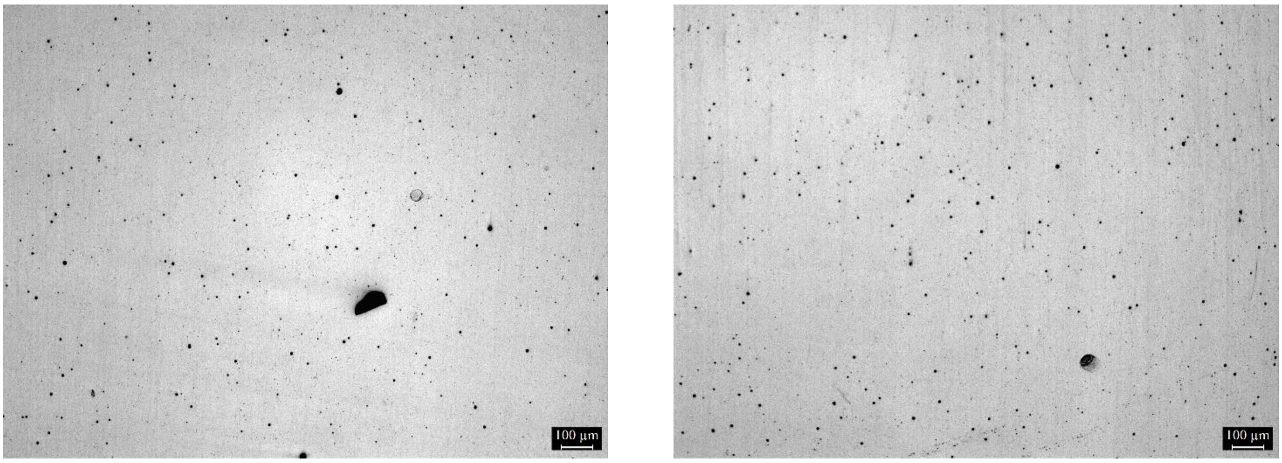

Fig. 5.30: polished Cube 1 at 50x magnification

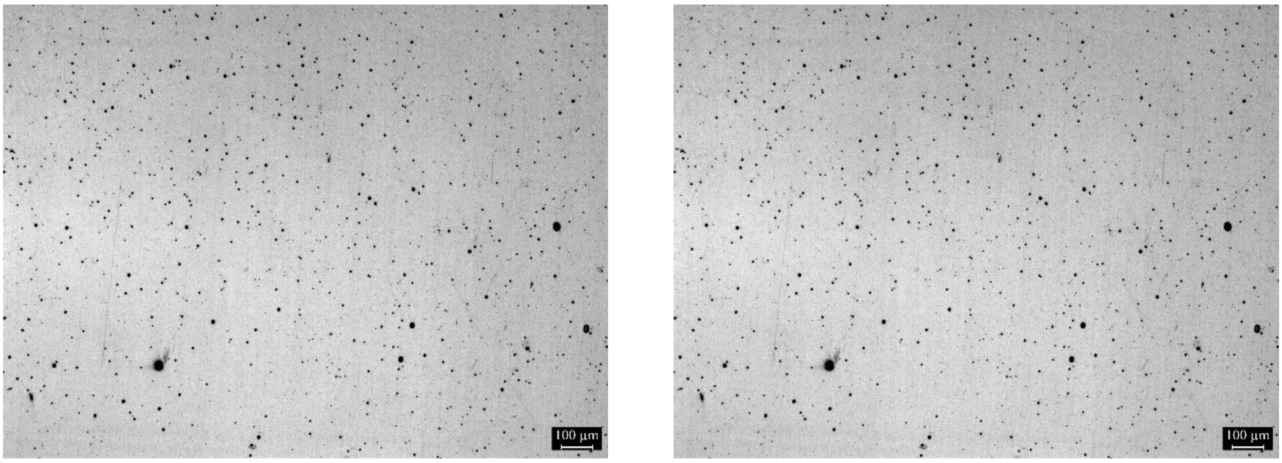

Fig. 5.31: polished Cube 2 at 50x magnification

The analyzed Cubes presents a lot of defects, keyholes and lack of fusion phenomena in the middle and in the bottom zone of the deposited material as reported in the Fig. 5.32 and Fig. 5.33. The presence of these defects could be explained by the low Laser Power level. The amount of energy supplied to the powder is not enough to completely melt the particles and creates these areas with enormous lack of powder fusion of almost 1 cm.

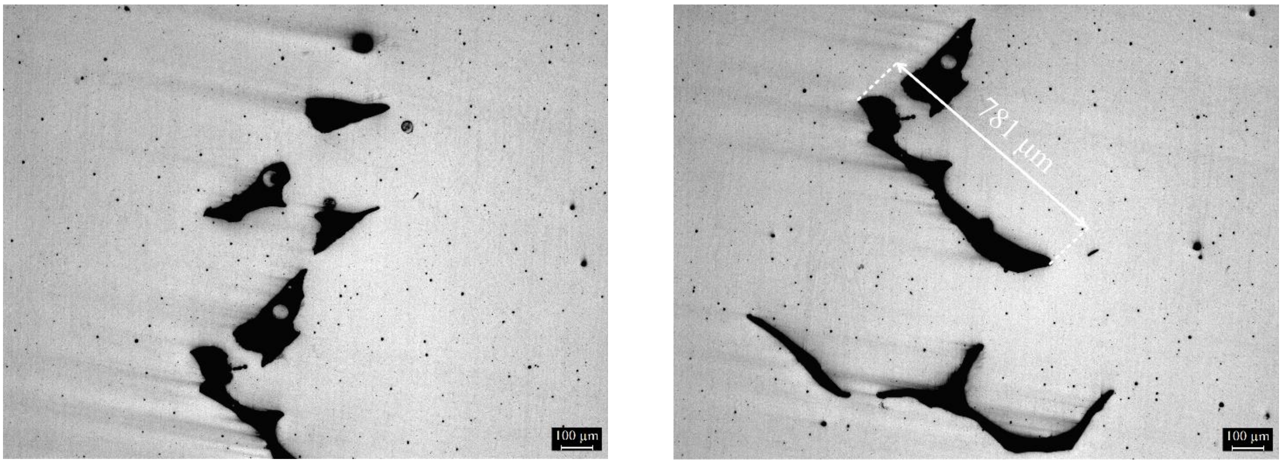

Fig. 5.32: Bulk n°1 defects at 50x magnification

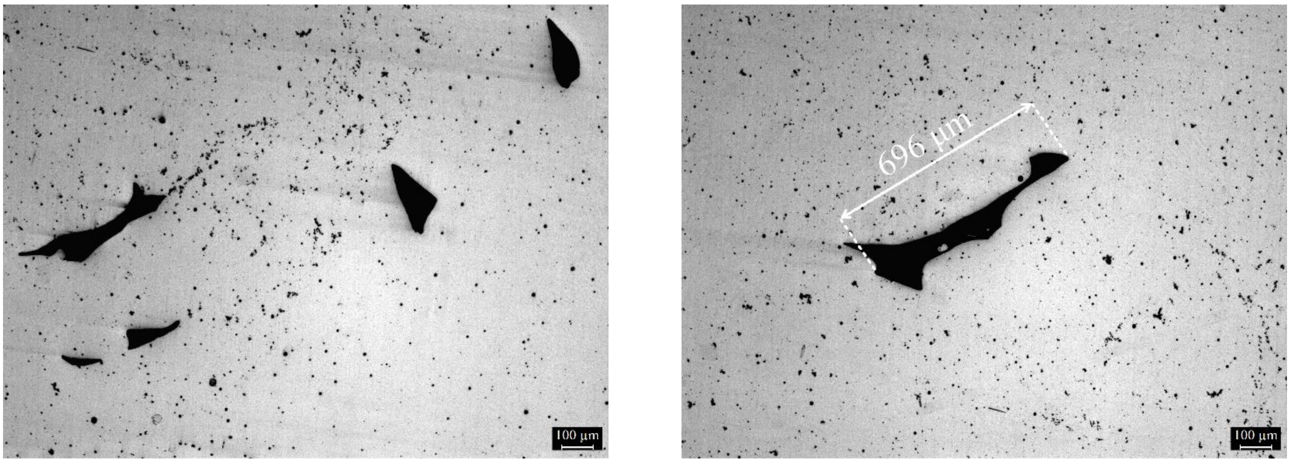

Fig. 5.33: Bulk n°2 defects at 50x magnification

5.4.2 Optical analysis of the etched Cubes

After the porosity and defect evaluations, the Cubes have been etched with the Kalling’s No.2 for 20 seconds to study the microstructure of the samples.

With this analysis we want to inspect the microstructure’s morphology and evaluate in a clear way the main grains growth phenomena associated with the DED process. In particular, the interaction with the substrate, the build top and edges have been analyzed with a 50x, 100x, 200x and 500x magnification.

In the following figures the Cubes structure is represented by three pictures for each of the main zone (bottom, middle and top) at a 50x magnification.

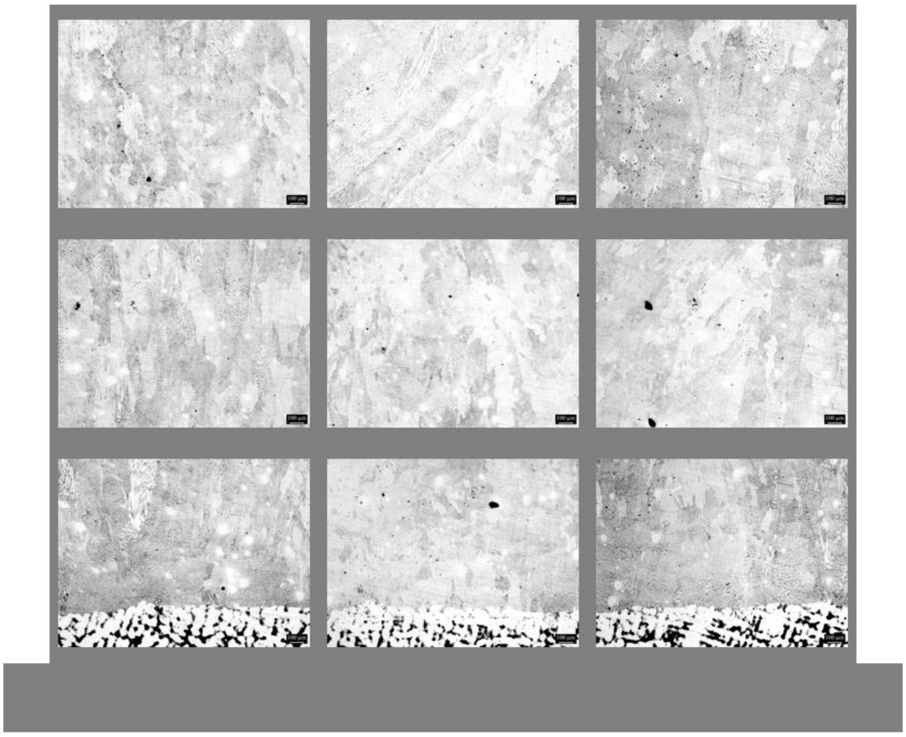

Fig. 5.34: etched Cube 1 at 50x magnification

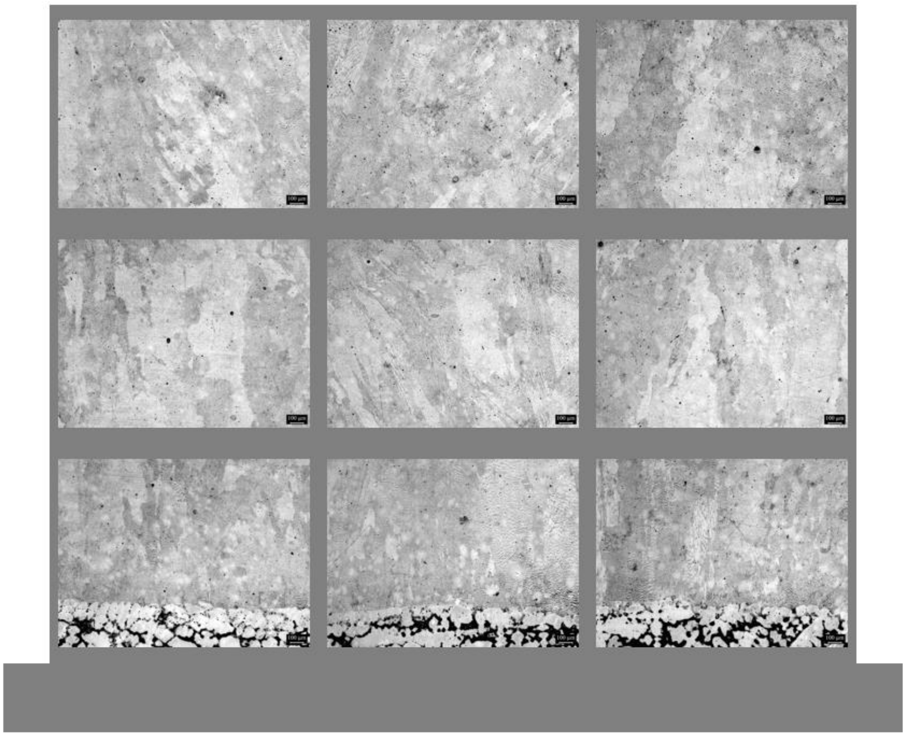

Fig. 5.35: etched Cube 2 at 50x magnification

5.4.2.1 Top of the Cubes

By analysing the top images, it is possible to notice a microstructural transition from the core to the top of the Cubes. The majority part of the sample is characterised by a large columnar grain growth that stops just before the part's surface and turns into an equiaxed microstructure. This phenomenon finds explanation in the thermodynamic of solidification that is governed by two main factors: the temperature gradient G and the solidification rate R that combine in the ratio "G/R" and in the cooling rate "GxR". Thanks to this parameter it is possible to define the size and shape of the microstructural feature. A reduction of G/R leads to an equiaxial growth while when the ratio increases, the solidifying dendrites tend to be more directional promoting an epitaxial growth. In the analysed Cubes, the temperature diminishes from the bottom to the top with a decrease of the local thermal gradient value and an increase in the G/R ratio involving a change in the microstructure solidification morphology. This phenomenon is showed in Fig. 5.36 where the transition from the columnar to the equiaxied microstructure seems clear.

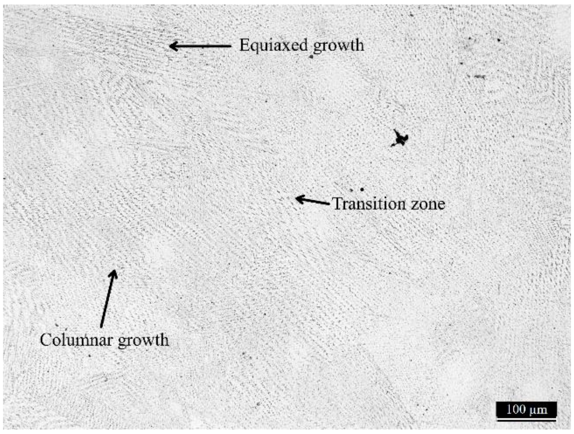

Fig. 5.36: microstructure of the etched Cube 1 at 100x magnification – transition from columnar to equiaxed microstructure

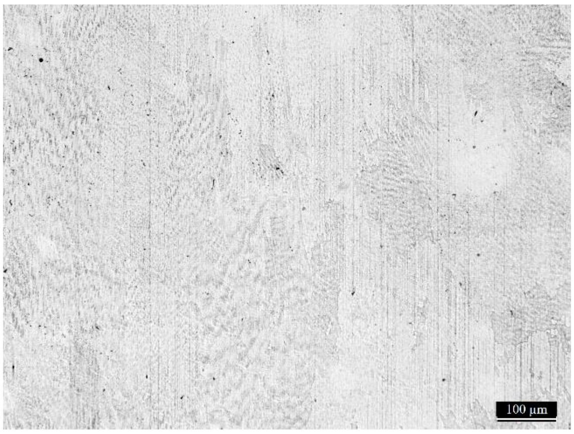

Fig 5.37: microstructure of the etched Cube 1 at 100x magnification – columnar grains just under the Top zone

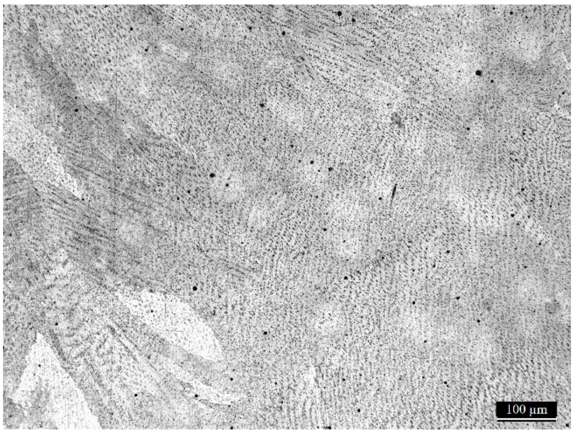

Fig. 5.38: microstructure of the etched Cube 2 at 100x magnification – transition from columnar to equiaxed microstructure

5.4.2.2 Core of the Cubes

The following images shows the core of the Cubes that present a prevalent columnar microstructural morphology. Unlike the Top zone, there is no transition to the equiaxial growth because the "G/R" ratio was significantly high during the solidification process. Cubes are printed using an offset contour deposition strategies which allows to obtain a more uniformly heat distribution if compared to the main deposition strategies (linear, zigzag, chessboard) (Ribeiro et al., 2020). A uniform heat distribution also brings a higher density as well as better height and width of the samples.

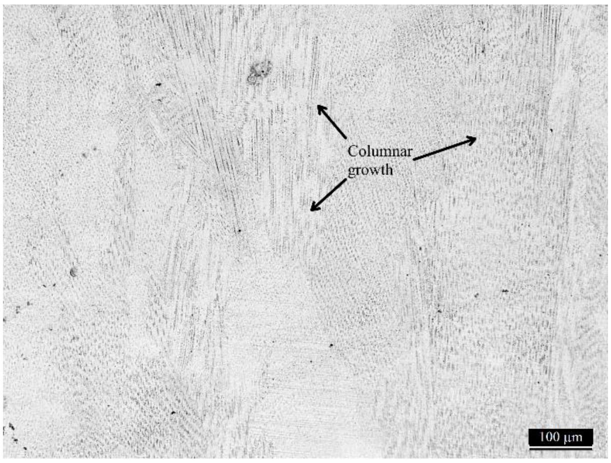

Fig. 5.39: microstructure of etched Cube 1 at 100x magnification – columnar grains growth in the core zone

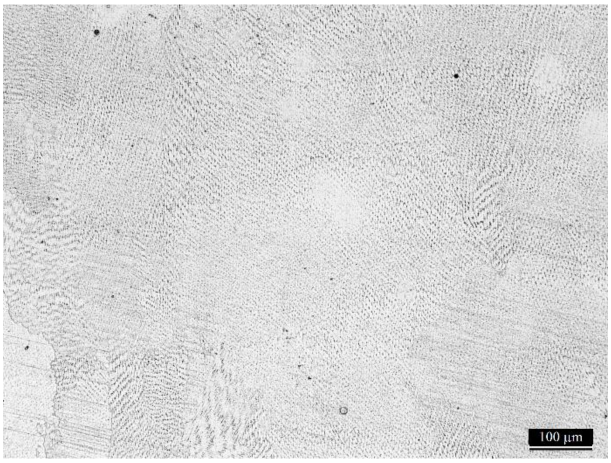

Fig. 5.40: microstructure of etched Cube 1 at 100x magnification – columnar grain growth in the core zone

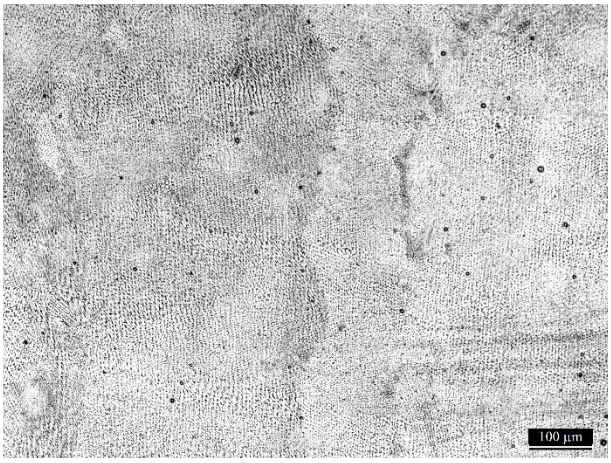

Fig. 5.41: microstructure of etched Cube 2 at 100x magnification – columnar grain growth in the core zone

5.4.2.3 Bottom of the Cubes

The interaction between the platform and the deposited material are very important for this thesis assignment in order to evaluate the applications of the DED technology for the repairing of high-performance metallic parts. As we can see from the following images, there are many lack of fusion in the middle of the bottom zone due to the low laser power level (Fig. 5.44 and Fig. 5.45). Moreover, were detected several melt pool's penetration of the substrate as shown in Fig 5.42 and Fig. 5.43. As a result of all this different defects it can be said that the coherence between the substrate and the deposited material was not achieved.

However, the microstructure present a large columnar grain growth as a result of high "G/R" values while Fig 5.46 show the presence of an equiaxed grain growth on the edge of the Cubes.

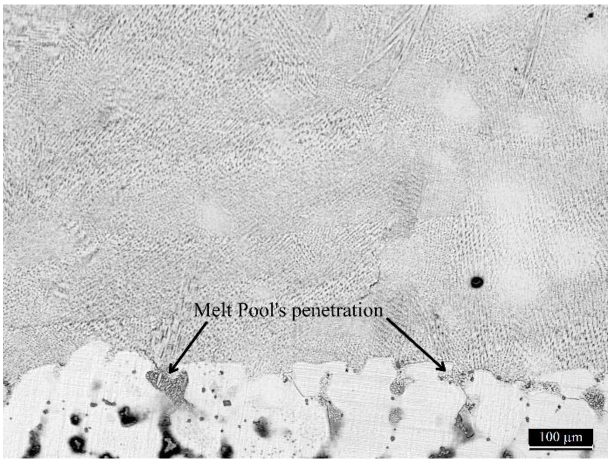

Fig. 5.42: microstructure of etched Cube 1 at 100x magnification – Melt Pool's base plate penetration

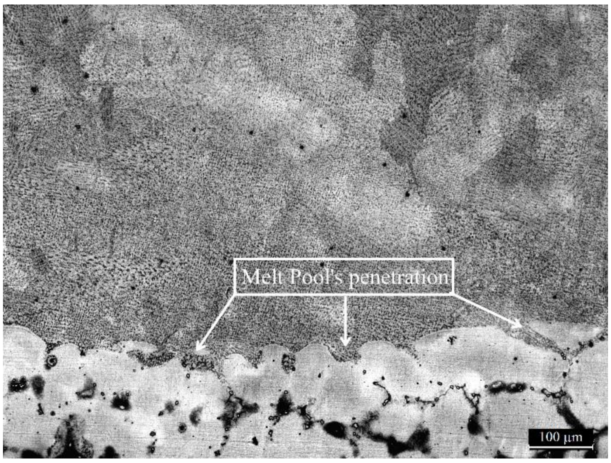

Fig. 5.43: microstructure of etched Cube 2 at 100x magnification – Melt Pool's base plate penetration

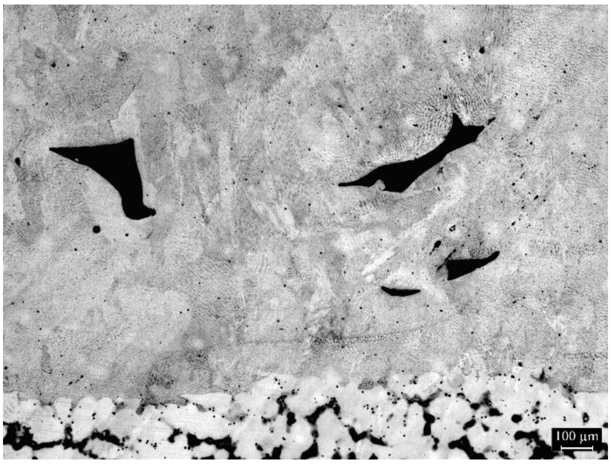

Fig. 5.44: microstructure of etched Cube 2 at 50x magnification – lack of fusion in the bottom zone

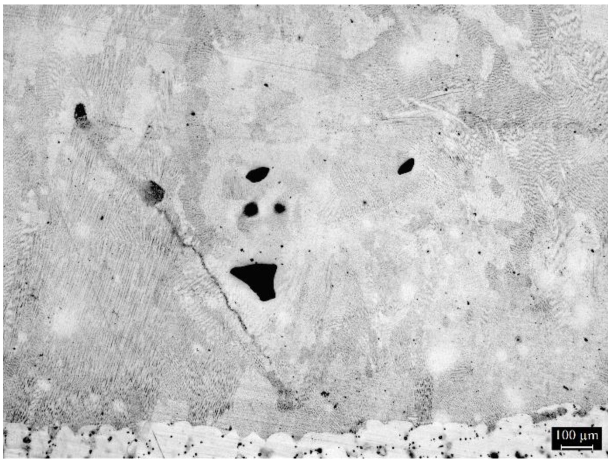

Fig. 5.45: microstructure of etched Cube 1 at 50x magnification – lack of fusion in the bottom zone

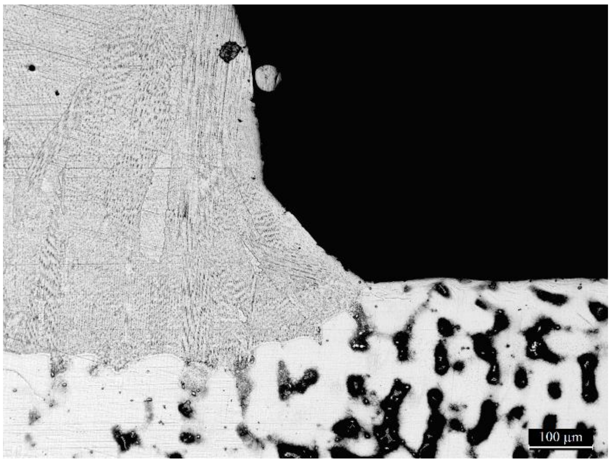

Fig 5.46: microstructure of etched Cube 1 at 100x magnification – equiaxed grain growth on the edge

Chapter 6

Conclusions

The focus of this thesis assignment was to identify the optimal process parameters for the Ni-based superalloys IN718, produced by Directed Energy Deposition, for the production and repair operations of aeronautical components. The results obtained from the analysed samples are reported in the following sections.

6.1 SSTs

The "On top" analysis revealed that:

- All the SSTs are regular in their profile and shape except no. 6, and 17 that present process instabilities.
- The higher laser power level (600 W) causes a pronounced HAZ width due to the severe interaction with the substrate.

The etched cross-section of the SSTs showed that:

- The presence of key hole in SSTs no. 1, 8, 11, 16, 19
- A remarkable Melt Pool's asymmetry in SSTs:
    - No. 3, 13, 14, 15, 26, 27 (P=600 W)
    - No. 5, 6, 17, 28 (P=500 W)
    - No. 9, 19, 31, 33 (P=400 W)
    - No. 36 (P=300 W)
- The analysis of the melt pool's main features depicted:
    - The increasing of Fusion Depth, Melt Pool's Width, and Bead Height as the Laser Power level increases at fixed Feed Rate.
    - The diminishing of the Bead Height as the Feed Rate level increases at fixed Laser Power level. However, the results of Fusion Depth and Melt Pool's Width are not so clear to establish a common trend.
    - The evaluated Melt Pools are not balanced in their geometry due to the low Laser Power level utilized to print the SSTs. These low values of P resulted in a "Fusion Depth/Width" and "Bead Head/Width" ratio far from the ideal value of "1". In particular, the "Bead Height/Width" value closest to the ideal one, obtained with P=600 W and F=600 mm/min, is more than five times higher.
    - The Feed Rate level does not plays a fundamental role in the "Fusion Depth/Width" and "Bead Head/Width" ratio evaluation.

- The adoption of low Laser Power level and medium-high Feed Rate is the best choice in terms of defect minimization.
- The adoption of high Laser Power level is fundamental to obtain the melt pool's features maximization.

6.2 SLs

After the optical analysis of the SLs' cross-section, "before etching", it is possible to say that:

- There are two different kinds of defects: "oxide" and "pore" that cannot be distinguished from each other and are considered as a single defect.
- The minimum defects percentage area of 0.019% is achieved by the layer D1 (P=300 W; F=600 mm/min).
- The minimum defects average size of 8.465 μm is achieved by the layer D3 (P=300 W; F=600 mm/min).
- The maximum defects percentage area of 0.116% is achieved by the layer A1 (P=700 W; F=800 mm/min).
- The maximum defects average size of 22.380 μm is achieved by the layer D1 (P=300 W; F=600 mm/min).
- Low Hatching Distance (HD=0.468 mm) and low Feed Rate values (F=600 mm/min) are the best choice in order to minimize the defect average size and percentage area.

After the optical analysis of the SLs' cross-section, "etched", it is possible to say that:

- Higher values of Bead Height and Fusion Depth are obtained at high Laser Power level (P=700 W) and at medium Feed Rate level (F=800 mm/min).
- High Laser Power level ensures a better coherence with the substrate while at low Laser Power levels there are some melt pool's penetration in the substrate.
- The Laser Power level of 700 W and the Feed Rate level of 800 mm/min ensures the best geometrical features while the trend of the Hatching Distance is not enough clear to establish an optimal value.

6.3 Cubes

The optical analysis of the Cubes' cross section, "before etching", shows:

- The presence of several keyhole and lack of fusion in the bottom zone of the samples due to the low Laser Power level used.
- A high defects percentage area of 0.891% in Cube 2.

The optical analysis of the Cubes' cross section, "etched", shows:

- Several melt pool's penetration of the substrate, which lead to a non-optimal coherence between substrate and deposited material. However, the HAZ is not very wide.
- An equiaxial growth at the edge of the Cubes and a columnar growth in the majority part of the samples.
- A transition zone separating the columnar growth of the inner part to the equiaxial growth situated on the edges.

Taking into account the obtained results, the optimal process parameters have been identified in P=700 W, F=800 mm/min and HD=0.468 mm.

References

Akram, J., Chalavadi, P., Pal, D., & Stucker, B. (2018). Understanding grain evolution in additive manufacturing through modeling. *Additive Manufacturing*, *21*(September 2017), 255–268. https://doi.org/10.1016/j.addma.2018.03.021

ASTM International. (2016). Standard Guide for Directed Energy Deposition of Metals. *ASTM Standard*, 1–22. https://doi.org/10.1520/F3187

Attaran, M. (2017). The rise of 3-D printing: The advantages of additive manufacturing over traditional manufacturing. *Business Horizons*, *60*(5), 677–688. https://doi.org/10.1016/j.bushor.2017.05.011

Bacciaglia, A., Ceruti, A., & Liverani, A. (2020). Additive Manufacturing Challenges and Future Developments in the Next Ten Years. In *Lecture Notes in Mechanical Engineering*. Springer International Publishing. https://doi.org/10.1007/978-3-030-31154-4_76

Bahnini, I., Rivette, M., Rechia, A., Siadat, A., & Elmesbahi, A. (2018). Additive manufacturing technology: the status, applications, and prospects. *International Journal of Advanced Manufacturing Technology*, *97*(1–4), 147–161. https://doi.org/10.1007/s00170-018-1932-y

Bogue, R. (2013). 3D printing: The dawn of a new era in manufacturing? In *Assembly Automation* (Vol. 33, Issue 4, pp. 307–311). https://doi.org/10.1108/AA-06-2013-055

Chen, B., & Mazumder, J. (2017). Role of process parameters during additive manufacturing by direct metal deposition of Inconel 718. *Rapid Prototyping Journal*, *23*(5), 919–929. https://doi.org/10.1108/RPJ-05-2016-0071

Control, Q. (n.d.). *Leica EZ4 and Leica EZ4 W.*

Di Falco, S. (2019). *Optimization of process parameters for Directed Energy Deposition (DED) of IN718 nickel-based superalloy*. https://webthesis.biblio.polito.it/12239/

Frazier, W. E. (2014). Metal additive manufacturing: A review. *Journal of Materials Engineering and Performance*, *23*(6), 1917–1928. https://doi.org/10.1007/s11665-014-0958-z

Gibson, I., Rosen, D., Stucker, B., Gibson, I., Rosen, D., & Stucker, B. (2015). Directed Energy Deposition Processes. In *Additive Manufacturing Technologies* (pp. 245–268). Springer, New York, NY. https://doi.org/10.1007/978-1-4939-2113-3_10

Goodfellow, A. J. (2018). Strengthening mechanisms in polycrystalline nickel-based superalloys. *Materials Science and Technology (United Kingdom)*, *34*(15), 1793–1808. https://doi.org/10.1080/02670836.2018.1461594

Hosseini, E., & Popovich, V. A. (2019). A review of mechanical properties of additively manufactured Inconel 718. *Additive Manufacturing*, *30*(August), 100877. https://doi.org/10.1016/j.addma.2019.100877

Hoyt, R. P., Cushing, J. I., Slostad, J. T., Jimmerson, G., Moser, T., Kirkos, G., Jaster, M. L., & Voronka, N. R. (2013). SpiderFab: An architecture for self-fabricating space systems. *AIAA SPACE 2013 Conference and Exposition*, 1–17. https://doi.org/10.2514/6.2013-5509

Johnson, A. S., Shao, S., Shamsaei, N., Thompson, S. M., & Bian, L. (2017). Microstructure, Fatigue Behavior, and Failure Mechanisms of Direct Laser-Deposited Inconel 718. *Jom*, *69*(3), 597–603. https://doi.org/10.1007/s11837-016-2225-2

Krassenstein, B. (n.d.). *20,000 3D Printed Parts Are Currently Used on Boeing Aircraft as Patent Filing Reveals Further Plans*. Retrieved February 23, 2021, from https://3dprint.com/49489/boeing-3d-print/

Kulkarni, A. (2018). Additive Manufacturing of Nickel Based Superalloys. *ArXiv*, 1–12. https://doi.org/10.31399/asm.hb.v24.a0006582

Laserdyne 430 | Primapower. (n.d.). https://www.primapower.com/laserdyne-430/#1448982719858-

0eaae0f8-b51dfc72-a00fae4f-fbacb154-86055a6d-1b9e

Leica DMI5000M. (n.d.). https://www.leica-microsystems.com/products/light-microscopes/p/leica-dmi5000-m/gallery/

Li, Y., Chen, K., & Tamura, N. (2018). Mechanism of heat affected zone cracking in Ni-based superalloy DZ125L fabricated by laser 3D printing technique. *Materials and Design*, *150*, 171–181. https://doi.org/10.1016/j.matdes.2018.04.032

Liu, F., Lin, X., Leng, H., Cao, J., Liu, Q., Huang, C., & Huang, W. (2013). Microstructural changes in a laser solid forming Inconel 718 superalloy thin wall in the deposition direction. *Optics and Laser Technology*, *45*(1), 330–335. https://doi.org/10.1016/j.optlastec.2012.06.028

Liu, R., Wang, Z., Sparks, T., Liou, F., & Newkirk, J. (2017). Aerospace applications of laser additive manufacturing. In *Laser Additive Manufacturing: Materials, Design, Technologies, and Applications* (pp. 351–371). Elsevier Inc. https://doi.org/10.1016/B978-0-08-100433-3.00013-0

Liu, S., & Shin, Y. C. (2019). Additive manufacturing of Ti6Al4V alloy: A review. *Materials and Design*, *164*, 107552. https://doi.org/10.1016/j.matdes.2018.107552

Maci, L. (2020). *Che cos'è l'Industria 4.0 e perché è importante saperla affrontare*. EconomyUp. https://www.economyup.it/innovazione/cos-e-l-industria-40-e-perche-e-importante-saperla-affrontare/

Mahamood, R. M., & Akinlabi, E. T. (2018). Effect of Powder Flow Rate on Surface Finish in Laser Additive Manufacturing Process. *IOP Conference Series: Materials Science and Engineering*, *391*(1). https://doi.org/10.1088/1757-899X/391/1/012005

Minet, K., Saharan, A., Loesser, A., & Raitanen, N. (2019). Superalloys, powders, process monitoring in additive manufacturing. In *Additive Manufacturing for the Aerospace Industry* (pp. 163–185). Elsevier Inc. https://doi.org/10.1016/B978-0-12-814062-8.00009-1

Najmon, J. C., Raeisi, S., & Tovar, A. (2019). Review of additive manufacturing technologies and applications in the aerospace industry. In *Additive Manufacturing for the Aerospace Industry* (pp. 7–31). Elsevier Inc. https://doi.org/10.1016/B978-0-12-814062-8.00002-9

Oh, W. J., Son, J. Y., Baek, G. Y., & Shim, D. S. (2020). Excess deposition for suppressing interfacial defects induced on parts repaired using direct energy deposition. *International Journal of Advanced Manufacturing Technology*, *106*(3–4), 1303–1316. https://doi.org/10.1007/s00170-019-04650-w

Prater, T. J., Bean, Q. A., Beshears, R. D., Rolin, T. D., Werkheiser, N. J., Ordonez, E. A., Ryan, R. M., & Ledbetter, F. E., I. (2016). *Summary Report on Phase I Results From the 3D Printing in Zero-G Technology Demonstration Mission, Volume I. I*(July).

Presi Mecatech 234. (n.d.). https://www.unitedscientific.co.za/images/Downloads/Presi/FT-MECATECH-234-264-GB-BD.pdf

Presi Mecatome T210. (n.d.). https://www.presi.com/en/product/mecatome-t210/

QATM Brillant 220. (n.d.). https://www.qatm.it/it/prodotti/taglio/modelli-da-banco/brillant-220/function-features/

Qi, H., Azer, M., & Ritter, A. (2009). Studies of standard heat treatment effects on microstructure and mechanical properties of laser net shape manufactured INCONEL 718. *Metallurgical and Materials Transactions A: Physical Metallurgy and Materials Science*, *40*(10), 2410–2422. https://doi.org/10.1007/s11661-009-9949-3

Remet IPA 30. (n.d.). https://www.microconsult.it/portfolio_page/inglobatrici-remet/

Ribeiro, K. S. B., Mariani, F. E., & Coelho, R. T. (2020). A Study of Different Deposition Strategies in Direct Energy Deposition (DED) Processes. *Procedia Manufacturing*, *48*, 663–670. https://doi.org/10.1016/j.promfg.2020.05.158

Sacco, E., & Moon, S. K. (2019). Additive manufacturing for space: status and promises. *International Journal of Advanced Manufacturing Technology*, *105*(10), 4123–4146. https://doi.org/10.1007/s00170-019-03786-z

Sciences, A., & Technologies, I. (n.d.). *SUPSI - Institute of Systems and Technologies for Sustainable Production - Ground Control*. https://www.supsi.ch/isteps_en/Laboratories/gruppo1/projects/Ongoing/progetto12

Singh, R., & Singh, S. (2017). Additive Manufacturing: An Overview. In *Reference Module in Materials Science and Materials Engineering*. Elsevier. https://doi.org/10.1016/b978-0-12-803581-8.04165-5

SLM Technology. (2009). *Material Data Sheet DMLS / SLM technology*. *2*, 99.

Thomas, D. A., Snyder, M. P., Napoli, M., Joyce, E. R., Shestople, P., & Letcher, T. (2017). Effect of acrylonitrile butadiene styrene melt extrusion additive manufacturing on mechanical performance in reduced gravity. *AIAA SPACE and Astronautics Forum and Exposition, SPACE 2017*, *203999*. https://doi.org/10.2514/6.2017-5278

Thompson, S. M., Bian, L., Shamsaei, N., & Yadollahi, A. (2015). An overview of Direct Laser Deposition for additive manufacturing; Part I: Transport phenomena, modeling and diagnostics. *Additive Manufacturing*, *8*, 36–62. https://doi.org/10.1016/j.addma.2015.07.001

Ünsal, I., Hirtler, M., Sviridov, A., & Bambach, M. (2020). Material properties of features produced from EN AW 6016 by wire-arc additive manufacturing. *Procedia Manufacturing*, *47*(2019), 1129–1133. https://doi.org/10.1016/j.promfg.2020.04.131

Wilson, J. M., Piya, C., Shin, Y. C., Zhao, F., & Ramani, K. (2014). Remanufacturing of turbine blades by laser direct deposition with its energy and environmental impact analysis. *Journal of Cleaner Production*, *80*, 170–178. https://doi.org/10.1016/j.jclepro.2014.05.084

Wimpenny, D. I., Pandey, P. M., & Jyothish Kumar, L. (2016). Advances in 3D Printing & additive manufacturing technologies. *Advances in 3D Printing and Additive Manufacturing Technologies*, 1–186. https://doi.org/10.1007/978-981-10-0812-2

Wu, B., Pan, Z., Ding, D., Cuiuri, D., Li, H., Xu, J., & Norrish, J. (2018). A review of the wire arc additive manufacturing of metals: properties, defects and quality improvement. *Journal of Manufacturing Processes*, *35*(August), 127–139. https://doi.org/10.1016/j.jmapro.2018.08.001

Yu, X., Lin, X., Liu, F., Wang, L., Tang, Y., Li, J., Zhang, S., & Huang, W. (2020). Influence of post-heat-treatment on the microstructure and fracture toughness properties of Inconel 718 fabricated with laser directed energy deposition additive manufacturing. *Materials Science and Engineering A*, *798*(August), 140092. https://doi.org/10.1016/j.msea.2020.140092

Zenou, M., & Grainger, L. (2018). Additive manufacturing of metallic materials. In *Additive Manufacturing: Materials, Processes, Quantifications and Applications* (pp. 53–103). Elsevier. https://doi.org/10.1016/B978-0-12-812155-9.00003-7

Thanks

Ringrazio la mia famiglia e i miei amici per avermi sempre supportato e sopportato durante questi lunghi anni di studi. Ringrazio la Prof.ssa Biamino per l’opportunità concessami nonostante le difficoltà che stiamo vivendo in questi tempi incerti. Ringrazio in particolare il Dr. Saboori per la pazienza, per gli indispensabili consigli e per avermi guidato nella stesura di questa tesi.

Un ringraziamento va ai miei amici e colleghi che mi hanno accompagnato in questo lungo viaggio condividendo gioie, successi e sacrifici.

Un ringraziamento in particolare va alla mia famiglia senza di cui non sarei dove sono ora.